Solid Earth, 16, 179–196, 2025
https://doi.org/10.5194/se-16-179-2025


Solid Earth Open Access EGU

# Petrogenesis of early Paleozoic I-type granitoids in the Longshoushan and implications for the tectonic affinity and evolution of the southwestern Alxa Block

**Renyu Zeng[1,2,3], Hui Su[1], Mark B. Allen[3], Haiyan Shi[4], Houfa Du[1,2], Chenguang Zhang[5], and Jie Yan[1,2]**

[1]School of Earth Sciences, East China University of Technology, Nanchang, 330013, China
[2]State Key Laboratory of Nuclear Resources and Environment, East China University of Technology, Nanchang 330013, China
[3]Department of Earth Sciences, Durham University, Durham DH1 3LE, UK
[4]Qinghai Geological Survey, Technology Innovation Center for Exploration and Exploitation of Strategic Mineral Resources in Plateau Desert Region, Ministry of Natural Resources, Xining 810000, China
[5]School of Geographic Sciences, Xinyang Normal University, Xinyang, 464000, China

**Correspondence:** Renyu Zeng (zengrenyu@126.com)

Received: 18 April 2024 – Discussion started: 26 June 2024
Revised: 18 December 2024 – Accepted: 9 January 2025 – Published: 26 February 2025

**Abstract.** In the Paleozoic, the Alxa Block was situated between the Central Asian Orogenic Belt and the North Qilian Orogenic Belt, and it experienced intense magmatic activity. Thus, the Alxa Block is an important area for understanding the tectonic framework and evolution of these two orogenic belts. However, there has long been debate regarding the tectonic affinity and tectonic evolution of the Longshoushan, located in the southwestern margin of the Alxa Block, during the Paleozoic. In this study, we present zircon U–Pb ages, whole-rock major and trace elements, and Hf isotopic data for the granitoids from the east of the Longshoushan to investigate these issues. Bulk-rock analyses show that these granitoids are weakly peraluminous, with high $SiO_2$ and $K_2O$ but low MgO, $TFe_2O_3$, and $P_2O_5$. They are also characterized by enrichment in LREE and LILE, depletion in HREE and HFSE, and a large range of $\varepsilon$Hf(t) values (monzogranite: $-0.3$ to $-16.2$; K-feldspar granite: 3.5 to $-7.7$). These geochemical features indicate that these granitoids are highly fractionated I-type granites, which were formed by crust- and mantle-derived magma mixing. LA-ICP-MS zircon U–Pb dating constrains the monzogranite and K-feldspar granite formed at $440.8 \pm 2.1$ Ma and $439.4 \pm 2.0$ Ma, respectively. Combining these results with previous chronological data, the geochronology framework of Paleozoic magmatic events in the Longshoushan is consistent with the North Qilian Orogenic Belt to the south but significantly differs from other parts of the Alxa Block and the Central Asian Orogenic Belt to the north. This result indicates that the Longshoushan was primarily influenced by the North Qilian Orogenic Belt during the early Paleozoic. Integrated with previous studies, a three-stage tectonic model is proposed of early Paleozoic accretion and arc magmatism leading to collision in the Longshoushan: (1) arc magmatism on an active continental margin with the northward subduction of the North Qilian back-arc basins (NQ bab; 460–445 Ma); (2) magmatic rocks, dominated by I-type granites, forming in a continent–continent collision setting, with significant crustal thickening interpreted as resulting from compressional stress and/or magmatic additions (445–435 Ma); (3) the development of abundant A-type granites and mafic dikes in response to extension, supported by a change in trace element chemistry indicating crustal thinning at this stage (435–410 Ma). This sequence of events and their timings is similar to other parts of the Central China Orogenic Belt and requires either a coincidence of several oceanic plates closing at the same time or an along-strike repetition of the same system.

**Published by Copernicus Publications on behalf of the European Geosciences Union.**

## 1 Introduction

The Alxa Block is a region of Precambrian basement adjacent to Phanerozoic orogenic belts (Fig. 1a). Its northern and southern sides are adjacent to the Central Asian Orogenic Belt and the North Qilian Orogenic Belt, respectively (Song et al., 2013; Xue et al., 2017; Zeng et al., 2016, 2021; Hui et al., 2021; Allen et al., 2023). The eastern margin may have undergone collision and amalgamation events with the North China Craton, although the timing of the amalgamation is in dispute (Li et al., 2012; Wang et al., 2015; Yuan et al., 2015; Dan et al., 2016). The Alxa Block therefore documents the tectonic evolution of the Proto-Tethys and Paleo-Asian oceans.

The Longshoushan is a mountain range located in the southern part of the Alxa Block (Fig. 1b) and is characterized by early Paleozoic magmatic activity. It is generally believed that the region to the northern part of the Longshoushan, known as the Beidashan, is mainly influenced by the Central Asian Orogenic Belt (Liu et al., 2016; Zhou et al., 2016), while the region to the south, the Hexi Corridor, is influenced by the North Qilian Orogenic Belt (Wei et al., 2013; Zhang et al., 2017). However, the tectonic background of the Longshoushan itself is still debated. Some researchers suggest that the early Paleozoic magmatic rocks in the Longshoushan are related to the subduction-accretionary orogenesis of the North Qilian Orogenic Belt (Liu et al., 2021; Zeng et al., 2021), while others propose a connection between these magmatic events and the rollback of the Paleo-Asian oceanic slab (Liu et al., 2016; Zhou et al., 2016; Xue et al., 2017). Furthermore, it is widely believed that the Longshoushan underwent a stress transition from a compressional to an extensional environment during the early Paleozoic (Zeng et al., 2016; Zhang et al., 2017; Wang et al., 2018; Liu et al., 2021). However, there are different viewpoints regarding the age of this transition, with some suggesting it occurred in the late Ordovician (∼ 450–440 Ma; Zhang et al., 2017; Liu et al., 2021) and others proposing it took place in the early Silurian (∼ 433–430 Ma; Yu et al., 2015; Zeng et al., 2016).

As an important component of the continental crust, granitoid is of great significance in studying crustal properties, tectonic framework, and tectonic evolution (e.g. Pearce et al., 1984; Li et al., 2014; Wang et al., 2017; Wu et al., 2017; Zeng et al., 2022). Extensive research has been conducted on granitoids in the Longshoushan, including the Zhimengou, Taohualashan, Jiling, Jinchuan, and Qingshanbao plutons and the western continuation of the Helishan area. However, research on the granitoids in the east of the Longshoushan has not yet been undertaken to the same extent. In this contribution, whole-rock geochemistry, zircon U–Pb ages, and Hf isotopes of the granitoids in the east of the Longshoushan are systematically studied. In conjunction with published data on Paleozoic magmatic rocks in the Longshoushan, this study also aims to investigate the tectonic background, crustal thickness variations, and tectonic evolution of the Longshoushan during the early Paleozoic.

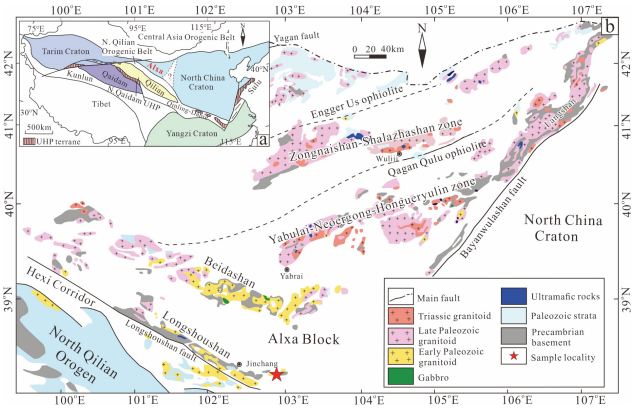


**Figure 1. (a)** Sketch geological map showing the tectonic location of the Alxa Block (modified from Song et al., 2013). **(b)** Simplified geological map of the Alxa Block Phanerozoic granitoids (modified from Zheng et al., 2014; Hui et al., 2021). AB – Alxa Block; CQB – Central Qilian Block; NCC- North China Craton.

## 2 Geological setting

The Alxa Block is separated from the Hexi Corridor and the Qilian Orogenic Belt by the Longshoushan Fault to the south; from the Tarim Craton by the Altyn Fault to the west (Zhang and Gong, 2018); and from the North China Craton by either the Bayanwulashan Fault, the western marginal fault of the Ordos Basin, or the Helanshan Fault to the east (Hui et al., 2021) (Fig. 1). On the northern margin of the Alxa Block, there are two important ophiolite belts: the Engger Us Ophiolite Belt in the north and the Qagan Qulu Ophiolite Belt in the south. Hf isotope data show that the magma sources of the Paleozoic magmatic rocks on both sides of the Qagan Qulu Ophiolite Belt are different (Zhang et al., 2015). Hence, recent studies have indicated that the Qagan Qulu Ophiolite Belt was most likely a late Paleozoic suture related to the closure of a back-arc basin, representing the tectonic boundary between the Alxa Block and the Central Asian Orogenic Belt (Shi et al., 2014; Zhang et al., 2015, 2023; Hui et al., 2021).

The tectono-thermal events in the Alxa Block mainly occurred during the Palaeoproterozoic and during the Paleozoic to early Mesozoic. During the Palaeoproterozoic, the Alxa Block experienced an ∼ 2.5 Ga magmatic–metamorphic event, ∼ 2.3 Ga and 2.05–2.0 Ga magmatic events, and a 1.95–1.80 Ga magmatic–metamorphic event (Zhang et al., 2013; Gong et al., 2016; Zeng et al., 2018; Qi et al., 2019; Wang et al., 2019). The ∼ 2.5 Ga magmatic–metamorphic event is relatively limited in distribution and is mainly reported in the Beidashan (Zhang et al., 2013) and the Longshoushan (Qi et al., 2019). The ∼ 2.3 Ga and 2.05–2.0 Ga magmatic events are primarily found in the Bayanwulashan,

Diebusuge, and Longshoushan areas, and they are generally believed to be related to an extensional tectonic setting (Dong et al., 2007; Dan et al., 2012; Zeng et al., 2018). The 1.95–1.80 Ga metamorphic events are widely documented in the metamorphic basement throughout the Alxa Block (Zhang et al., 2013; Gong et al., 2016; Zeng et al., 2018). It is generally believed to be associated with a late Palaeoproterozoic orogeny (Gong et al., 2016; Zeng et al., 2018), possibly recording the amalgamation of the North China Craton (Zhang et al., 2013; Zeng et al., 2018).

During the Paleozoic to early Mesozoic, the Alxa Block was mainly influenced by the Central Asian Orogenic Belt to the north and the North Qilian Orogenic Belt to the south, resulting in extensive magmatic activities. Zhang and Gong (2018) divided the magmatic activities during this period into three stages: 460–390 Ma, 360–300 Ma, and 299–230 Ma. These magmatic activities in the Alxa Block generally exhibited a progressive younging trend from south to north. Compared to the other two stages, the 460–390 Ma magmatic events were relatively limited in distribution within the Alxa Block. They were mainly developed in the central southern parts of the Alxa Block, such as the Beidashan and Longshoushan areas, and in the eastern regions like the Yamatu and Langshan areas. The tectonic settings of the 460–390 Ma magmatism in the Alxa Block are not fully understood. Some researchers believe that 460–390 Ma magmatic events are related to the subduction of oceanic crust related to the Central Asian Orogenic Belt (Liu et al., 2016; Zhou et al., 2016; Xue et al., 2017). For example, Xue et al. (2017) suggest that these rocks are a result of the slab rollback of the Paleo-Asian oceanic slab, while Zhou et al. (2016) propose a connection with post-arc rifting. However, some work suggests that the 460–390 Ma magmatic events in the southern margin of the Alxa Block, particularly in the Longshoushan, are related to the North Qilian Orogenic Belt (Zeng et al., 2016, 2021; Zhang et al., 2017; Liu et al., 2021). Additionally, some researchers suggest that the 460–390 Ma magmatic events in the eastern part of the Alxa Block are the product of collision and accretion between the Alxa Block and the North China Craton (Wang et al., 2015; Dan et al., 2016).

The magmatic events during the periods of 360–300 Ma and 299–230 Ma are widely distributed in the Alxa Block, especially in the Yabulai–Nuorigong–Hongqueryulin zone and the Beidashan. The predominant rock type is granite, with subordinate gabbroic rocks (e.g. Zhang and Gong, 2018; Dan et al., 2014; Zhang et al., 2016). These two periods of magmatic events are generally believed to be associated with the subduction–collision and post-collisional evolution of the Central Asian Orogenic Belt (Zhang and Gong, 2018; Liu et al., 2017).

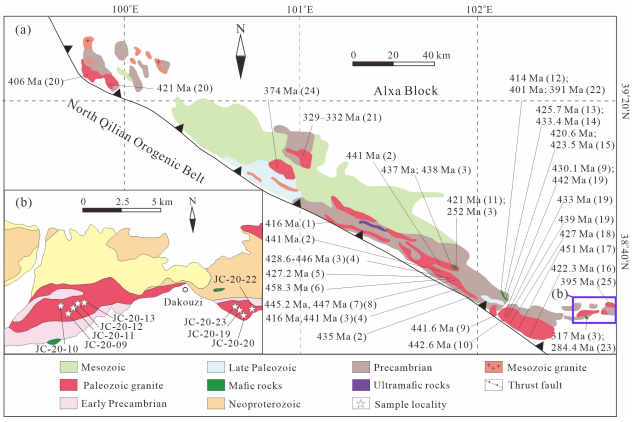


**Figure 2. (a)** Simplified geological map of the southwestern Alxa Block (Wang et al., 2020). **(b)** Simplified geological map of the east of the Longshoushan area. Data are in Table S1 in the Supplement (all age data were obtained using the zircon U–Pb method).

## 3 Samples and petrography

In this study we investigated two plutons located in the east of the Longshoushan (Fig. 1b), including monzogranite and K-feldspar granite. These two plutons occupy an area of approximately 12 $km^2$. In the study area, the early Precambrian Longshoushan Complex, Neoproterozoic Dunzigou Formation, Hanmushan Formation, and Neogene strata are well exposed (Fig. 2). The Longshoushan Complex is mainly composed of biotite quartz schist and migmatite, while the Dunzigou Formation and Hanmushan Formation are marine clastic and carbonate sedimentary rocks. The monzogranite and K-feldspar granite both intruded into the early Precambrian Longshoushan Complex (Fig. 2). Four samples of monzogranite and four samples of K-feldspar granite were collected at locations shown in Fig. 2b.

### 3.1 Monzogranite

The monzogranite is generally pale red in colour with a fine- to medium-grained texture (Fig. 3a). The mineral assemblage contains K-feldspar (∼ 32 %), plagioclase (∼ 28 %), quartz (∼ 35 %), and biotite (∼ 5 %), as well as accessory minerals such as magnetite, zircon, and apatite. K-feldspar grains are euhedral or subhedral, always exhibit grid twinning (Fig. 3b), and can contain rounded quartz and plagioclase inclusions (Fig. 3c). Plagioclase commonly shows polysynthetic twinning and is altered to sericite and carbonate, with rims surrounded by newly formed K-feldspar (Fig. 3b). Biotite is the main dark mineral, occurring in flaky shapes and filling in the interstices between the other minerals, with embayment features and chloritization (Fig. 3b).

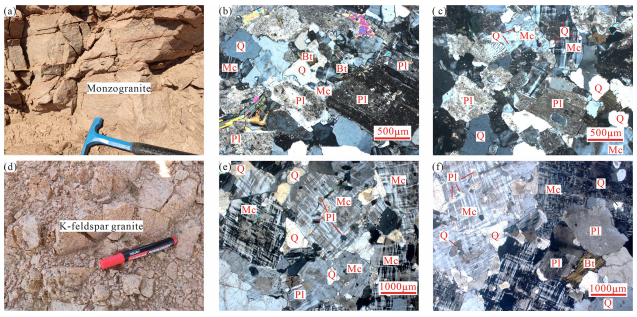


**Figure 3.** Field photographs and photomicrographs of monzogranite **(a, b, c)** and K-feldspar granite **(d, e, f)**, with panels **(b–c)** and **(e–f)** in perpendicular polarized light. Q – quartz; Kfs – K-feldspar; Pl – plagioclase; Mc – microcline; Bt – biotite.

### 3.2 K-feldspar granite

The K-feldspar granite is generally pale red in colour with a medium-grained texture (Fig. 3d). The mineral assemblage contains K-feldspar (∼ 55 %), quartz (∼ 30 %), plagioclase (∼ 10 %), and biotite (∼ 5 %), as well as accessory minerals such as apatite, magnetite, and zircon. K-feldspar has a grain size range between 3 to 4 mm, mainly composed of microcline with grid twinning and containing numerous plagioclase and quartz inclusions (Fig. 3e). Plagioclase usually exhibits polysynthetic twinning and has sericitization and carbonatization. Euhedral to subhedral crystals are tabular-shaped. The main dark mineral is biotite; grains have embayed crystal margins and chloritization (Fig. 3f).

## 4 Analytical methods

Representative rock samples were selected for geochemical analysis. The analyses of whole-rock major and trace elemental compositions were conducted at Analytical Chemistry & Testing Services (ALS) Chemex (Guangzhou) Ltd by using X-ray fluorescence (XRF) (ME-XRF26) and ICP-MS (ME-MS81), respectively. The detailed methods are given in Zeng et al. (2022).

Cathodoluminescence (CL) imaging of zircon was performed at Chengpu Geological Testing Co. Ltd, Langfang, China, using a TIMA. The LA-ICP-MS zircon U–Pb dating and trace element analyses were carried out at Wuhan Sample Solution Analytical Technology Co., Ltd., Wuhan, China. The laser ablation system used is the COMPexPro 102 ArF excimer laser (wavelength of 193 nm and maximum energy of 200 mJ) with a spot size of 35 µm and a repetition rate of 8 Hz. The ICP-MS is the Agilent 7900. Zircon 91500 and glass NIST610 were used as external standards for U–Pb dating and trace element calibration, respectively. GJ-1 and Plešovice were used for quality control. In the experiment, the weighted mean ages of GJ-1 and Plešovice were $600.3 \pm 3.7$ Ma ($n = 7$, MSWD $= 0.04$) and $337.5 \pm 3.0$ Ma ($n = 4$, MSWD $= 0.03$), respectively. In this paper, the $^{206}Pb/^{238}U$ and $^{207}Pb/^{206}U$ ages are determined for younger zircons (< 1000 Ma) and older grains (> 1000 Ma). The detailed methods are given in Zong et al. (2017).

Zircon in situ Lu–Hf analyses were undertaken at the Wuhan Sample Solution Analytical Technology Co., Ltd, Hubei, China, using a Neptune Plus MC-ICP-MS. An ArF excimer laser ablation system of GeoLas HD was used with 44 µm spot size. The detailed analytical programme is the same as that outlined by Hu et al. (2012). In order to ensure the reliability of the analysis data, three international zircon standards of Plešovice, 91500, and GJ-1 were analysed simultaneously with the actual samples. During our analyses, the values of Plešovice, 91500, and GJ-1 were 0.282472–0.282495, 0.282302–0.282314, and 0.282024–0.282032, respectively, consistent with their recommended values (Plešovice: $0.282482 \pm 23$; 91500: $0.282308 \pm 106$; GJ-1: $0.282010 \pm 89$; Zhang et al., 2020).

## 5 Analytical results

The data for major and trace elements, zircon U–Pb ages, zircon trace elements, and zircon Hf isotopes are shown in Tables S2, S3, S4, and S5, respectively.

### 5.1 Geochemical characteristics

#### 5.1.1 Monzogranite

The samples of monzogranite have $SiO_2$ contents ranging from 71.59 wt % to 72.05 wt %. They have low $Na_2O$ (3.75 wt %–3.88 wt %) and high $K_2O$ (4.40 wt %–4.52 wt %). All samples fall in the granite area in the TAS classification (Fig. 4a) and the alkali-calcic to calc-alkaline series areas in the $SiO_2 - N_2O + K_2O$ diagram (Fig. 4b). Contents of $Al_2O_3$ are 14.40 wt %–14.47 wt %, and contents of A/KNC are 1.05–1.07. All compositions fall in the weakly peraluminous field of the A/NC−A/KNC diagram (Fig. 4c).

The $La_N/Yb_N$ values of monzogranite range from 22.26 to 27.84, showing enrichment of LREE and depletion of HREE. On chondrite-normalized REE patterns (Fig. 5c), the monzogranite has relatively inclined LREE patterns and flat HREE patterns. All the samples display negative Eu anomalies ($\delta$ Eu = 0.73–0.75) and slightly positive Ce anomalies ($\delta$ Ce = 0.99–1.22). In the primitive mantle-normalized trace element diagram (Fig. 5d), these samples show enrichment of LILEs (e.g. Rb and K), depletion of HFSEs (e.g. Nb, Ta, Ti, and P), and no depletion of Hf and Zr.

#### 5.1.2 K-feldspar granite

The samples of K-feldspar granite have $SiO_2$ contents from 75.77 wt % to 76.18 wt %. They have low $Na_2O$ (3.09 wt %–3.13 wt %) and high $K_2O$ (5.54 wt %–6.18 wt %). All sam-

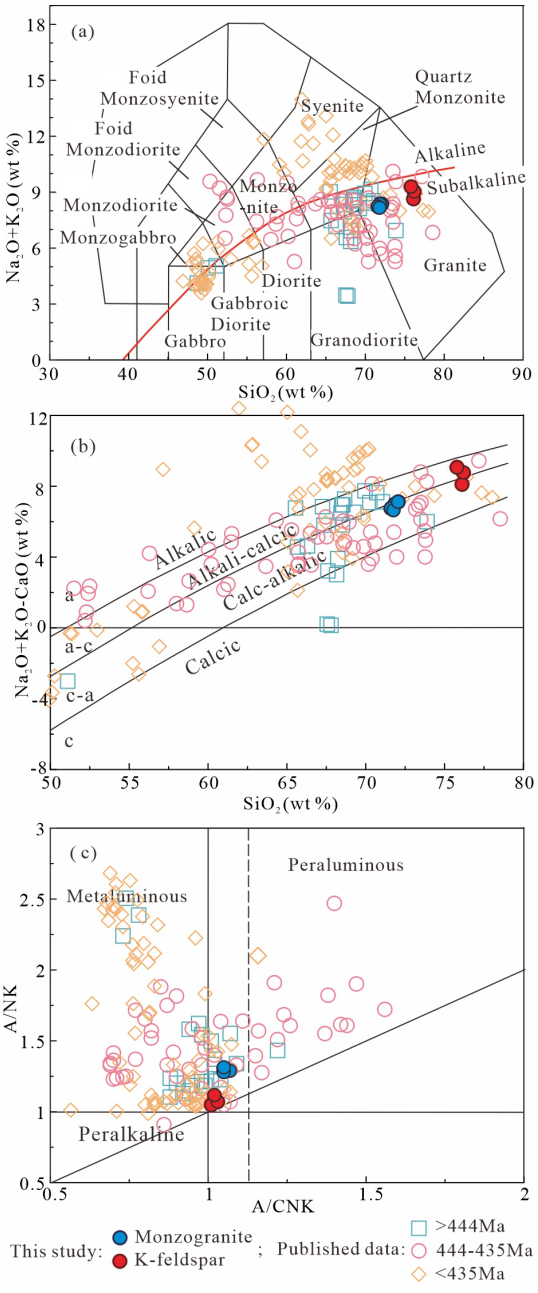


**Figure 4.** Geochemical classification diagrams. **(a)** TAS diagram (after Middlemost, 1994). **(b)** A/CNK−A/NK diagram (after Maniar and Piccoli, 1989). **(c)** $Na_2O + K_2O - CaO$ vs. $SiO_2$ diagram (after Frost et al., 2001). The source of the published data can be found in Table S1.

ples fall in the granite area in the TAS classification (Fig. 4a) and the alkali-calcic series and calc-alkaline series areas in the $SiO_2 - N_2O + K_2O$ diagram (Fig. 4b). Contents of $Al_2O_3$ are 12.33 wt %–12.36 wt %, contents of A/KNC are 1.01–1.03, and all samples are weakly peraluminous in the A/NC−A/KNC diagram (Fig. 4c).

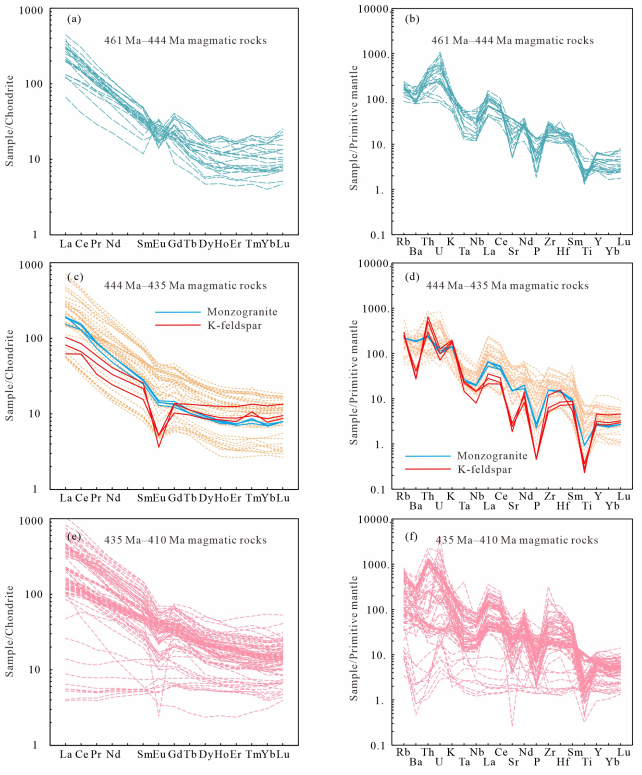


**Figure 5.** Chondrite-normalized REE patterns and primitive mantle-normalized trace element patterns for early Paleozoic magmatic rocks (chondrite and primitive mantle values are from Sun and McDonough, 1989). The source of the published data can be found in Table S1.

The $La_N/Yb_N$ values of K-feldspar granite samples are from 6.38 to 11.94, showing enrichment of LREE and depletion of HREE. On chondrite-normalized REE patterns (Fig. 5c), the K-feldspar granite has relatively inclined LREE patterns and flat HREE patterns. All samples display clear negative Eu anomalies ($\delta$Eu = 0.19–0.41) and slightly positive Ce anomalies ($\delta$Ce = 1.08–1.35). In the primitive mantle-normalized trace element diagram (Fig. 5d), these samples show enrichment of LILEs (e.g. Rb, Ba, and K), strong depletion of HFSEs (e.g. Nb, Ta, Ti, and P), and no depletion of Hf and Zr.

## 5.2 Zircon U–Pb geochronology, trace elements, and Hf isotopes

### 5.2.1 Monzogranite

Zircons from monzogranite (JC-20-9) are mostly euhedral, transparent, colourless, and 80–160 µm in length. The zircons have bright CL intensity and oscillatory zoning in the CL images (Fig. 6a), with Th/U ratios of 0.10–1.27. A total of 25 spots cluster on the concordia curve with $^{206}Pb/^{238}U$ ages of 429–449 Ma, defining a weighted mean age of 440.8 ± 2.1 Ma (MSWD = 1.6) (Fig. 6a, b).

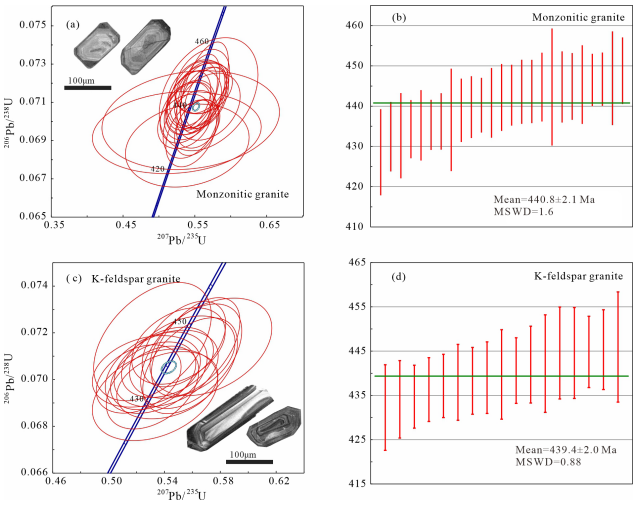


**Figure 6.** Concordia diagrams for zircon LA-ICP-MS U–Pb analyses.

We analysed 16 zircons for REE. The spots have a ΣREE of 704–2660 ppm (average 1270 ppm), a ΣLREE of 18–212 ppm (average 89 ppm), a ΣHREE of 623–2550 ppm (average 1181 ppm), a ΣLREE/ΣHREE of 0.02–0.17, a $\delta$Eu of 0.12–0.38 (average 0.24), and a $\delta$Ce of 1.16–125.04 (average 18.38). On chondrite-normalized REE patterns (Fig. S1), these spots show depletion of LREEs, enrichment of HREEs, and clear negative Eu anomalies and positive Ce anomalies.

We analysed 15 zircons for Lu–Hf isotopes. The zircons have $^{176}Hf/^{177}Hf$ ranging from 0.282295 to 0.282617, with $\varepsilon$Hf(t) of 3.72 to −7.83 and a two-stage Hf isotope depleted mantle model age ($T_{DM2}$) of 1187 to 1917 Ma, calculated by using the weighted mean age.

### 5.2.2 K-feldspar granite

Zircons from K-feldspar granite (JC-20-19) are mostly euhedral, transparent, colourless, and 80–130 μm in length and have bright CL intensity and oscillatory zoning (Fig. 6c) with Th/U ratios of 0.29–1.01. Among these, 17 spots cluster on the concordia curve with $^{206}Pb/^{238}U$ ages of 432–446 Ma, defining a weighted mean age of 439.4 ± 2.0 Ma (MSWD = 0.88) (Fig. 6c, d), while 7 spots have ages of 825–2344 Ma. Among them, 3 zircons are weakly luminescent and lack discernible internal structure, with Th/U ratios of 0.03–0.09. and $^{207}Pb/^{206}Pb$ ages of 1857, 1847, and 1894 Ma, respectively. There are 3 zircons with bright CL intensity and oscillatory zoning, with Th/U ratios of 0.48–1.00 and $^{207}Pb/^{206}Pb$ ages of 2216, 2344 and 2307 Ma, respectively.

A total of 13 zircon spots, which define the weighted mean age of 439.4 ± 2.0 Ma, have a ΣREE of 542–1414 ppm (average 862 ppm), a ΣLREE of 26–260 ppm (average 80 ppm), a ΣHREE of 502–1154 ppm (average 783 ppm), a ΣLREE/ΣHREE of 0.04–0.23, a $\delta$Eu of 0.15–0.58 (average 0.34), and a $\delta$Ce of 1.78–129.07 (average 20.97). All the spots show depletion of LREEs, enrichment of HREEs, and clear negative Eu anomalies and positive Ce anomalies.

A total of 13 zircons were analysed for Lu–Hf isotopes from sample JC-20-19. Altogether, 12 spots, which define the weighted mean age of 439.4 ± 2.0 Ma, show $^{176}Hf/^{177}Hf$ and $\varepsilon$Hf(t) values of 0.282494 to 0.282056 and −0.49 to −16.27, respectively, with a $T_{DM2}$ of 1453 to 2446 Ma calculated by using the weighted mean age. The remaining older zircon (825 Ma) has a $^{176}Hf/^{177}Hf$ ratio of 0.281812, with $\varepsilon$Hf(t) of −16.07, and $T_{DM2}$ of 2722.

## 5.3 Discussion

## 6 Formation age

In this study, zircons from the monzogranite and K-feldspar granite can be divided into two groups (I-type and II-type; Fig. 7a). The I-type zircons (the zircons from the monzogranite and the majority of zircons from the K-feldspar granite) have high Th/U ratio values (0.10–1.27) and bright intensity and oscillatory zoning in the CL images. The above characteristics are consistent with those of igneous zircon (Hoskin and Schaltegger, 2003). Hence, the weighted mean ages of 440.8 ± 2.1 Ma (MSWD = 1.6) and 439.4 ± 2.0 Ma (MSWD = 0.88) are taken to represent the magmatic emplacement ages of monzogranite and K-feldspar granite, respectively. Four analyses from sample JC-20-9 have $^{207}Pb/^{206}Pb$ ages of 825, 2216, 2307, and 2344 Ma, which are much older than the emplacement ages of the K-feldspar granite. Hence, these zircons are captured or inherited magmatic zircons. The II-type zircons (spots #2, #20, and #22 from JC-20-9) have low Th/U ratio values (0.03–0.09), are weakly luminescent, and lack discernible internal structure in the CL images, which suggests that their ages most likely represent the timing of metamorphism (Hoskin and Schaltegger, 2003). The spots from the II-type zircons have ages of 1847–1894 Ma, which is consistent with the age of the metamorphic events in the Longshoushan area during the Palaeoproterozoic (Gong et al., 2016; Zeng et al., 2018).

## 6.1 Crystallization conditions

Temperature, oxygen fugacity, and pressure are important indicators for the crystallization conditions of magmatic rocks. They play a significant role in investigating the origin and evolution of magmas and their relationship with mineralization processes (Xiao et al., 2017; Zeng et al., 2022).

Zircon saturation thermometry ($T_{Zrn}$) and the Ti-in-zircon thermometer ($T_{Zr-Ti}$) are commonly used methods for estimating magma temperatures. Based on the calculation method introduced by Watson and Harrison (1983), the $T_{Zrn}$ values for the monzogranite and K-feldspar granite are in the ranges of 839–842 °C (with an average value of 840 °C) and

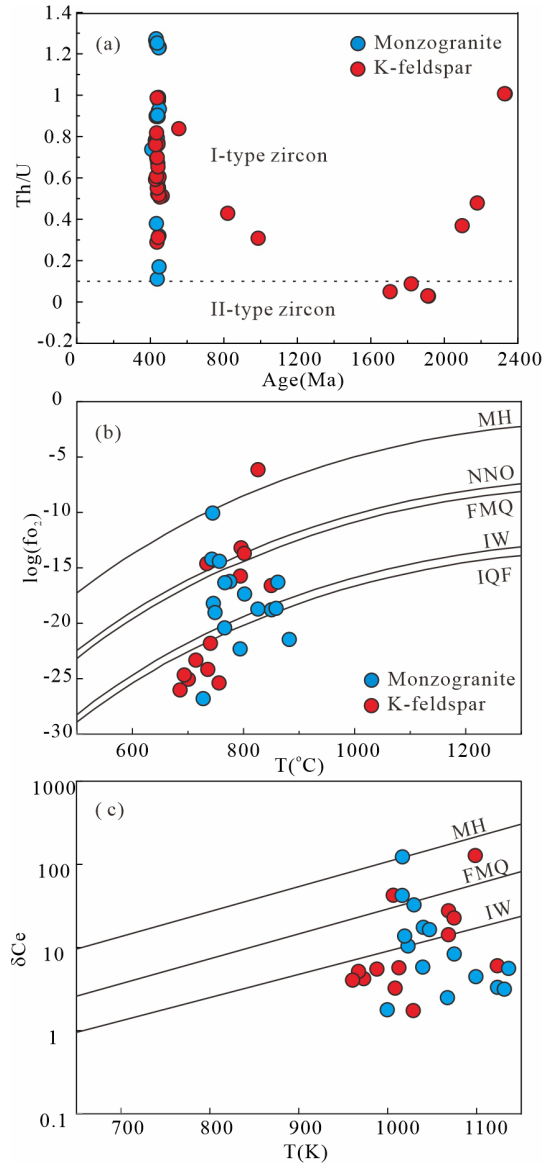


**Figure 7.** Age-Th/U **(a)**, $T$-log($fO_2$) **(b)**, and $T$-$\delta$Ce **(c)** diagrams of zircon.

745–817 °C (with an average value of 782 °C), respectively. The solubility of Ti in zircon is related to the temperature during zircon formation and to the activities of $TiO_2$ ($aTiO_2$) and $SiO_2$ ($aSiO_2$) in the melt (Watson and Harrison, 2005; Ferry and Watson, 2007). Since both monzogranite and K-feldspar granite contain abundant quartz and zircon but rare ilmenite and xenotime, the $aSiO_2$ and $aTiO_2$ are 1 and 0.5, respectively (Schiller and Finger, 2019). According to the calculation method proposed by Ferry and Watson (2007), the Ti temperatures of 16 autocrystic zircons from the monzogranite range from 727 to 883 °C (with an average of 791 °C), while the Ti temperatures of 13 autocrystic zircons from the K-feldspar granite range from 687 to 851 °C (with an average of 756 °C). In addition, the $Al_2O_3/TiO_2$ ratio of the whole rock can be used as an indicator of the formation temperature of granites (Hui et al., 2021). Hot granites typically have lower $Al_2O_3/TiO_2$ ratios, while cold granites have higher $Al_2O_3/TiO_2$ ratios (Sylvester, 1998). The samples of monzogranite have lower $Al_2O_3/TiO_2$ ratios (72.0 to 72.4) than those of the samples of K-feldspar granite (154.5 to 246.6), implying that the melts of monzogranite are hotter than those of K-feldspar granite. This result is consistent with the outcomes obtained from zircon saturation thermometry ($T_{Zrn}$) and the Ti-in-zircon thermometer.

Due to the distinct partitioning behaviour of $Ce^{4+}$ and $Ce^{3+}$ in zircon, the cerium in zircon can reflect the oxygen fugacity condition of the magmatic systems (Trail et al., 2012). Using the formulas proposed by Trail et al. (2012), the logfO2 for the monzogranite and K-feldspar granite falls within the ranges of $-27$ to $-10$ (with an average of $-18$) and $-26$ to $-6$ (with an average of $-19$), respectively. In the log$fO_2$-$T$ (°) and Ce/Ce*-$T$ (K) diagrams (Fig. 7b and c), the monzogranite and the K-feldspar granite mostly fall below the FMQ buffer, indicating low oxygen fugacity conditions.

Generally, when garnet is the dominant residual phase in the source region, the melt that forms will exhibit a significant inclined HREE distribution pattern, with $Y/Yb > 10$ and $Ho/Yb > 1.2$ characteristics (Tang et al., 2021). In this study, the HREE distribution patterns of the monzogranite and K-feldspar granite are relatively flat, with Y/Yb ranging from 7.91 to 10.93 and Ho/Yb ranging from 0.33 to 0.38, indicating that garnet is not the dominant residual phase. Therefore, the pressure of the granite source region should be less than 1.7 GPa (mostly less than 1.5 GPa; Tang et al., 2021). The Yb contents of the monzogranite and the K-feldspar granite are both less than 2 ppm (except for one sample), and the Sr contents of the two plutons are both less than 400 ppm, indicating the characteristics of low Yb and low Sr granite (Zhang et al., 2006). In addition, these two plutons have the characteristic low $Al_2O_3$ contents and a distinctly negative Eu anomaly. These features are consistent with the low Sr and low Yb granites in northern Hebei, implying that the monzogranite and the K-feldspar granite are partial melts of high-pressure granulites containing plagioclase, clinopyroxene, garnet, and amphibole at the bottom of the thickened lower crust (Li et al., 2004; Zhang et al., 2006), with source pressures estimated to be between 0.8 and 1.5 GPa (Zhang et al., 2010).

### 6.2 Granitoid petrogenesis

The monzogranite and K-feldspar granite have low Zr (58–175 ppm), Ce (37.6–94.5 ppm), $Zr + Nb + Ce + Y$ (129.6–296.9 ppm), and FeO*/MgO (4.3–12.2), distinct from typical A-type granites ($Zr > 250$ ppm, $Ce > 100$ ppm, $Zr + Nb + Ce + Y > 350$ ppm, and FeO*/MgO > 16; Whalen et al., 1987). In addition, the magma temperature of the monzogranite ($T_{Zrn}$: 839–842 °C; $T_{Zr-Ti}$: 728 to

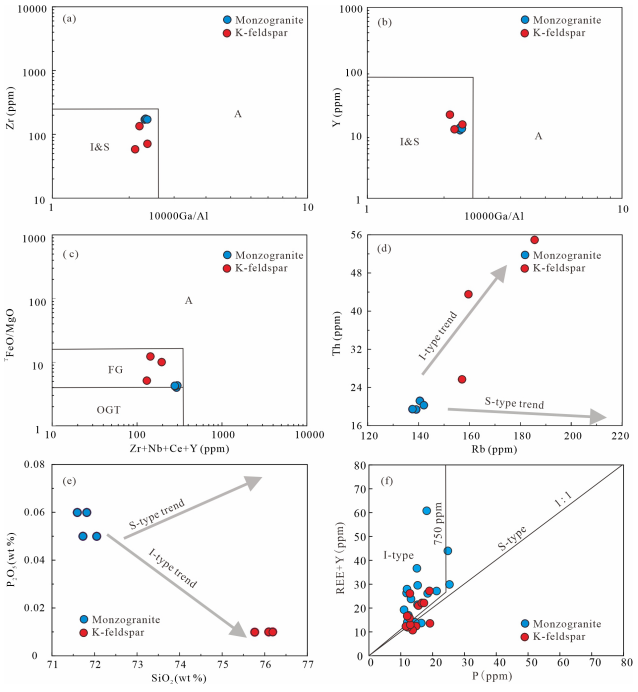


**Figure 8.** Discrimination diagram of granitoid genetic types. **(a, b, c)** 10 000 Ga/Al vs. Zr, 10 000 Ga/Al vs. Y, and Zr + Nb + Ce + Y vs. TFeO/MgO (after Whalen et al., 1987). **(d)** Rb vs. Th. **(e)** $SiO_2$ vs. $P_2O_5$. **(f)** P vs. REE + Y (after Burnham and Berry, 2017).

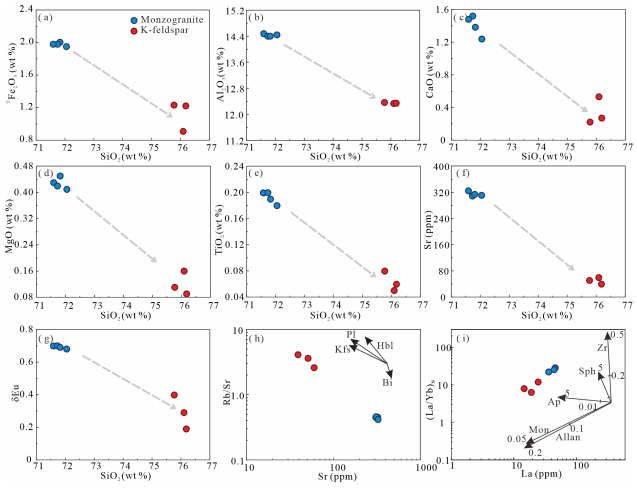


**Figure 9.** $SiO_2$ vs. major element oxides **(a–e)**, $SiO_2$ vs. Sr **(f)**, Sr vs. Rb/Sr **(h)**, Sr vs. Ba **(g)**, and La vs. $(La/Yb)_N$ **(i)** for the Dakouzi pluton (the partition coefficients of Rb, Sr, and Ba are from Philpotts and Schnetzler, 1970; the partition coefficients of La and Yb are from Ewart and Griffin, 1994). Pl – plagioclase; Kfs – K-feldspar; Bt – biotite; Zr – zircon; Sph – sphene; Ap – apatite; Mon – monazite; Allan – allanite.

883 °C) and K-feldspar granite ($T_{Zrn}$: 745–817 °C; $T_{Zr-Ti}$: 687 to 851 °C) is significantly lower than that of typical A-type granite (> 900 °C; Skjerlie and Johnston, 1992). Furthermore, all compositions fall in the region of I- and S-type granite rather than the A-type granite in the discrimination diagrams (Fig. 8a–c). Thus, the monzogranite and K-feldspar granite are not A-type granites and are more compatible with being I- or S-type granites. The samples of monzogranite and K-feldspar granite have A/CNK < 1.1 and normative corundum < 1 % in the CIPW norm calculation, and there is no presence of peraluminous minerals, such as cordierite, andalusite, muscovite, and garnet, which is distinctly different from the mineralogy of S-type granites (Chappell and White, 1992). As shown in Th–Rb and $SiO_2$–$P_2O_5$ diagrams (Fig. 8d and e), the positive trend between Th and Rb and the negative trend between $P_2O_5$ and $SiO_2$ also demonstrate the evolutionary trend of typical I-type granite (Wolf and London, 1994; Kong et al., 2018; Liu et al., 2021). Moreover, in the P-(REE + Y) diagram (Fig. 8f), autocrystic zircons in both the monzogranite and the K-feldspar granite have lower P concentrations, and the concentration of P and REE + Y does not show an obvious positive correlation, showing the characteristics of zircons in I-type granite rather than S-type granite.

As noted, the monzogranite and K-feldspar granite have a close temporal and spatial relationship, similar $Na_2O + K_2O$ contents (Fig. 4a), and uniform REE and trace element patterns (Fig. 5c, d). These characteristics suggest a co-magmatic origin. The genesis of highly fractionated I-type granite has been proposed to two primary mechanisms: (1) fractional crystallization (FC) or assimilation fractional crystallization (AFC) of mantle-derived mafic magmas (He et al., 2019) and (2) partial melting of crustal materials with involvement of some mantle-derived components, accompanied by subsequent fractional crystallization (Karsli et al., 2010; Liu et al., 2021).

Mantle-derived primary melt would be expected to have high MgO, $TFe_2O_3$, CaO, and Cr contents (Ma et al., 2013), which are obviously inconsistent with the characteristics of the monzogranite and K-feldspar granite in this study. Furthermore, mafic melts can only form a minor volume of granitic melts through crystal differentiation, with a proportion of about 9 : 1 (Zeng et al., 2016). However, in the Longshoushan, most of the ∼ 440 Ma magmatic rocks are granitic rocks, and no large-scale exposures of mafic–ultramafic rocks have been reported. Therefore, monzogranite and K-feldspar granite are unlikely to have been formed by the FC or AFC processes of mantle-derived magma.

The Hf isotopes of zircon are not affected by fractional crystallization and thus can provide precise constraints on the origin of magma (Griffin et al., 2002). The zircon $\varepsilon$Hf(t) values of the monzogranite range from −0.37 to −16.28, while those of the K-feldspar granite range from 3.53 to −7.74, both exhibiting a large range of $\varepsilon$Hf(t) (Fig. 10). This phenomenon indicates the existence of different Hf isotopic end-members in the source regions of these two plutons, which could be attributed to the mixing of mafic and felsic melts

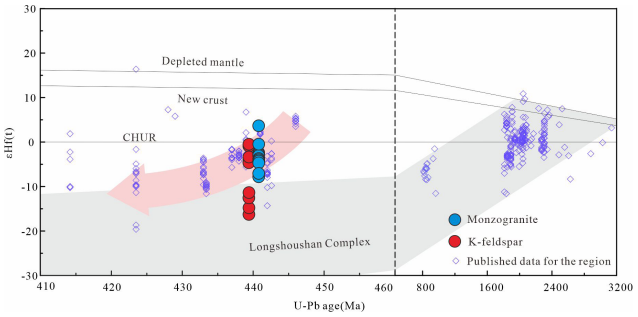


**Figure 10.** Zircon $\varepsilon$Hf(t)-age (Ma) diagram for samples in this study and published data for the region. The source of the published data can be found in Table S1 (the red arrow represents the variation trend in $\varepsilon$Hf(t)).

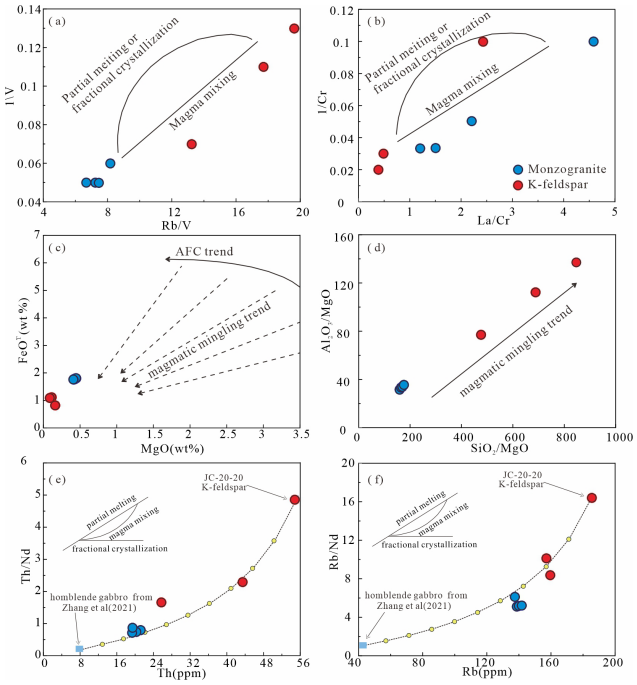


**Figure 11.** Diagram of magma mixing discrimination. **(a)** Rb/V vs. 1/V diagram; **(b)** La/Cr vs. 1/Cr diagram; **(c)** MgO vs. $FeO^T$ diagram; **(d)** $SiO_2$/MgO vs. $Al_2O_3$/MgO diagram; **(e)** Th vs. Th/Nd diagram; **(f)** Rb vs. Rb/Nd diagram (**a** and **b** after Schiano et al., 2010; **e** after Zorpi et al., 1989).

(Zhang et al., 2015; He et al., 2019), heterogeneous composition of source crust materials (Zeng et al., 2016), or variable degrees of melting of source minerals (Zeng et al., 2021). In addition, some quartz and biotite boundaries have been melted and transformed into irregular embayments, and plagioclase inclusions occur within the quartz. These observations suggest the injection of high-temperature magma during the magma evolution process (Duan et al., 2021). On the Rb/V−1/V and La/Cr−1/Cr diagrams (Fig. 11a and b), samples from monzogranite and K-feldspar granite exhibit a linear trend, indicating magma mixing (Liu et al., 2021). On the MgO–$FeO_T$ and $SiO_2$/MgO−$Al_2O_3$/MgO diagrams (Fig. 11c and d), our samples also show an obvious magma-mingling trend (Tang et al., 2021). In addition, in the Longshoushan, Zhang et al. (2021) reported an age of ∼441 Ma for the Xijing clinopyroxene diorite vein, and Wang et al. (2019) reported crystallization ages of ∼440 Ma for the mantle-derived mafic micro-granular enclaves in the Jiling granite. Therefore, there was mantle-derived magmatism in the Longshoushan at ∼440 Ma, which could provide the mantle material for the granitic magmatism. We use the ∼441 Ma Xijing clinopyroxene diorite (Zhang et al., 2021) and our sample of K-feldspar granite (JC-20-20) to assess magma mixing simply in terms of two end-member compositions. Our simulation results show a curvilinear evolutionary relationship on the Th/Nd–Th and Rb/Nd–Rb diagrams (Fig. 11e and f), which is also consistent with magma mixing (Schiano et al., 2010; Tang et al., 2021). To conclude, the monzogranite and K-feldspar granite in this study were derived by the magma mixing of mantle- and crust-derived magmas.

In crust–mantle mixing processes, crust-derived magmas typically have lower $\varepsilon$Hf(t) values. Therefore, lower $\varepsilon$Hf(t) values can roughly reflect the composition of the crustal source. As shown in Fig. 10, some spots with lower $\varepsilon$Hf(t) values from both rock bodies fall within the evolutionary trend line of the early Precambrian basement strata, known as the Longshoushan Complex, into which the studied plutons are intruded. Furthermore, abundant 1.85–1.90 Ga metamorphic zircons and ∼2.3 Ga plutons have been identified in the Longshoushan Complex (Gong et al., 2016; Zeng et al., 2018), which corresponds to the inherited zircon ages found in the K-feldspar granite. Therefore, the Longshoushan Complex is mostly likely the crustal source of the granitoids in this study. Compared with the K-feldspar granite, the monzogranite has higher $\varepsilon$Hf(t) values and is closer to the mantle end-member in the mixing diagrams, indicating a relatively lower proportion of crust-derived magmas.

All the samples of the monzogranite and the K-feldspar granite are characterized by relatively high $SiO_2$, total alkali, and differentiation index; low $TFe_2O_3$, MgO, and CaO contents; low Nb/Ta (9.5–14.5) and Zr/Hf values (26.3–40.2); and enrichment of Rb, Th, and U, indicating that these rocks are highly fractionated (Xiao et al., 2014; Wu et al., 2017). This is consistent with the samples of these two granites being in the fractionated felsic granites (FGs) area in the $FeO^T$/MgO vs. Zr + Nb + Ce + Y diagram (Fig. 8c). In this study, the granitoids have negative Eu–Ba–Sr anomalies (Fig. 5c and d), indicating plagioclase and K-feldspar fractionation (Harris et al., 1990). In the Rb/Sr vs. Sr diagrams (Fig. 9g), the granitoid samples show a separation trend of plagioclase. The negative correlation of $SiO_2$ with TFeO and MgO suggests fractionation of amphibole and biotite during magmatic evolution (Fig. 9a and d). As shown in the Sr–Ba

diagram (Fig. 9h), amphibole is likely to dominate the fractional phase. The increasing $TiO_2$ content with decreasing $SiO_2$ (Fig. 9e), along with the clear Ti, Nb, and Ta anomalies in the primitive-mantle-normalized trace element diagrams (Fig. 5b), implies the fractionation of rutile (Foley et al., 2000). In a diagram of $(La/Yb)_N$ vs. La (Fig. 9i), the variation in REE contents suggests the fractionation of monazite and allanite. Hence, the monzogranite and K-feldspar granite have experienced extensive fractional crystallization of plagioclase, K-feldspar, amphibole, biotite, rutile, monazite, and allanite.

### 6.3 Tectonic implications

#### 6.3.1 Tectonic affinity of the Longshoushan in the Paleozoic

During the Paleozoic–Mesozoic, the Alxa Block was situated between multiple tectonic domains, with its northern and southwestern sides experiencing subduction-accretionary orogenesis of the Central Asian Orogenic Belt and the North Qilian Orogenic Belt, respectively (Song et al., 2013; Liu et al., 2017; Xue et al., 2017; Zhang and Gong et al., 2018; Hui et al., 2021). The North Qilian Orogenic Belt is a component of the much larger Central China Orogenic Belt, which extends ∼ 2000 km east and west of the Alxa Block.

It is widely believed that the Yabulai–Nuoergong–Hongglueryulin zone and the Zongnaishan–Shalazhashan zone at the northern side of the Alxa Block were mainly influenced by the Central Asian Orogenic Belt (Li et al., 2017; Liu et al., 2017; Sun et al., 2017; Zhang and Gong et al., 2018; Hui et al., 2021). As shown in Fig. 13a, magmatic activities in these areas were mainly concentrated in the late Paleozoic–Mesozoic, with a peak age of ∼ 270 Ma. The magmatic activity in the Longshoushan, which lies at the southern margin of the Alxa Block, mainly occurred in the early Paleozoic with a peak age of ∼ 440 Ma (Fig. 12d), which is significantly different from the magmatic events on the northern side of the Alxa Block and basically consistent with the Hexi Corridor, North Qilian Orogenic Belt, and Central Qilian Block (Fig. 12e–g), as well as the wider Central China Orogenic Belt (Allen et al., 2023). Therefore, the Longshoushan was most likely part of the evolution of the Central China Orogenic Belt during the Paleozoic and specifically adjacent regions of the North Qilian Orogenic Belt and the Hexi Corridor. There is a small amount of late Paleozoic magmatic rock in the Longshoushan, such as the Taohualashan pluton (Xue et al., 2017). These plutons are mainly distributed on the northwestern side of the Longshoushan (Fig. 1b), close to the northern boundary of the Alxa Block (near the Central Asian Orogenic Belt), and are considered to be related to the Central Asian Orogenic Belt (Xue et al., 2017; Zhang et al., 2021). The Beidashan is located to the north of the Longshoushan, and both early Paleozoic and late Paleozoic–Mesozoic magmatic rocks are extensively exposed there (Fig. 12c). This feature indicates that the Beidashan is located at the intersection of two tectonic domains and was influenced by both the Central Asian Orogenic Belt and the North Qilian Orogenic Belt. In addition, similarly to the Longshoushan, the early Paleozoic magmatic rocks in the Beidashan are mainly distributed on the southeastern side, while the Paleozoic–Mesozoic magmatic rocks are mainly distributed on the northwestern side (Fig. 1b). Therefore, in the Alxa Block, the Longshoushan and the southeastern side of the Beidashan are mainly influenced by the North Qilian Orogenic Belt, while other areas to the north are mainly influenced by the Central Asian Orogenic Belt. Apart from Beidashan and Longshoushan, early Paleozoic magmatic rocks are mainly distributed in the eastern part of the Alxa Block, including the Bayan Nuru, Bayanwulashan, and Langshan areas. Various authors suggested that these magmatic events are related to the convergence between the Alxa Block and the North China Craton (Dan et al., 2016; Wang et al., 2015).

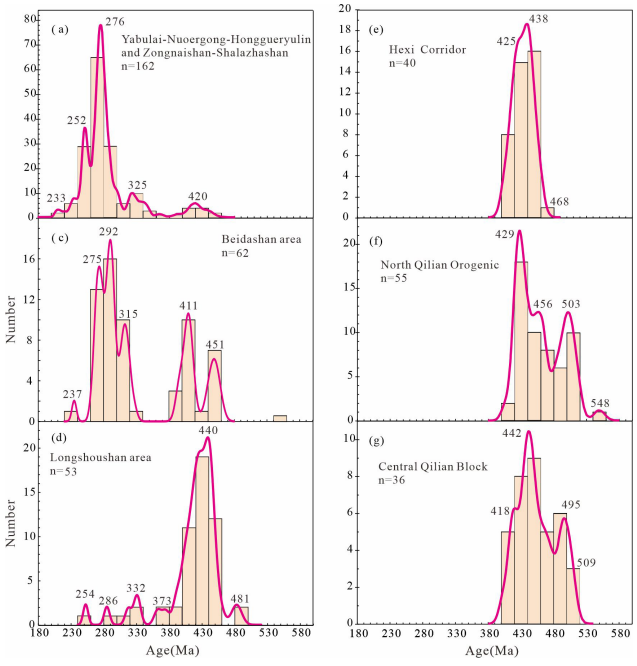


**Figure 12.** Kernel density estimate (KDE) plots for Palaeozoic and Mesozoic magmatic ages in the Alxa Block, North Qilian Belt, and Central Qilian Block. Ophiolitic rocks are not included. Data are in Table S1. All dates are zircon U–Pb ages (histogram bin width is 20).

Figure 12 indicates that magmatism in the Alxa Block started later than 500 Ma, which is later than in other parts of the Central China Orogenic Belt to the south. In addition, the Longshoushan area lacks the twin peaks in early Paleozoic ages for magmatism found in other areas, such as the North Qilian Orogenic Belt and Central Qilian Block, at ∼ 500 and 430 Ma (Allen et al., 2023). We suggest that the reason for these differences in age spectrum is that the Longshoushan was initially far enough away from the Proto-

Tethyan subduction zone that it was not affected by arc magmatism, which was focused on the North Qilian Orogenic Belt and the Central Qilian Block to the south. A detailed discussion can be found in Sect. 6.4.3.

### 6.3.2 Evaluation of crustal thickness

Hu et al. (2017) designed an empirical formula between the median Sr/Y ratio of intermediate–acid rocks and the crustal thickness in continental collisional orogens. In addition, Mantle and Collins (2008) designed the empirical relationship between the maximum Ce/Y ratio of basalt and crustal thickness. Therefore, Sr/Y and Ce/Y ratios of magmatic rocks can be used as proxies for crustal thickness. The Longshoushan experienced the convergence and collision of the Alxa Block and the basement of the North Qilian Orogenic Belt in the early Paleozoic, so the intermediate–acid rocks and basic–ultrabasic rocks formed in this process can be used to estimate the thickness of the palaeo-crust by using the formulas designed by Hu et al. (2017) and Mantle and Collins (2008), respectively.

In this study, we collected published data for 153 magmatic rock samples of early Paleozoic age in the Longshoushan, including 8 ultrabasic rock samples, 31 basic rock samples, 45 intermediate rock samples, and 88 acidic rock samples. According to the location, lithology, and formation age of these rocks, the above samples are divided into 31 subsets in this study. Among them, 26 subsets of intermediate–acid rocks were run through the data processing scheme recommended by Hu et al. (2017) to process data. The first step is to eliminate the samples with $SiO_2 > 72\,\%$ and $MgO < 0.5\,\%$ or $> 6.0\,\%$ in each subset, thereby removing those that exceed the range of original data fitting the formula. The second step is to remove individual data points with Sr/Y outliers from each data subset using the modified Thompson tau statistical method. The third step is to eliminate the subset whose average Rb/Sr value is greater than 0.35, in order to filter out samples that have been strongly affected by fractionation. After the above process, there are 6 subsets of 32 samples left. According to the calculation formula of Hu et al. (2017), the crustal thickness is calculated by the median ratio of Sr/Y in each subset of samples. On the other hand, 5 subsets of basic–ultrabasic rock samples were processed by the Mantle and Collins (2008) method. The first step is to eliminate the samples with $SiO_2 < 44\%$, $MgO < 4\%$, and $LOI > 4\%$. In the second step, samples of alkaline and shoshonitic basalts derived from the enriched lithospheric mantle are excluded, as these rocks typically have abnormally high Ce/Y ratios ($> 4$), rendering the results unusable. After the above process, there are 4 groups of 28 samples left. According to the calculation formula of Mantle and Collins (2008), the corresponding crustal thickness is obtained through the maximum Ce/Y ratio in each subset; see Table S6 for the calculation results. As shown in Fig. 13, the thickness of the crust underwent a transition from thickening to thinning during the period of 460–410 Ma, with the initial timing of the transition being ∼ 435 Ma.

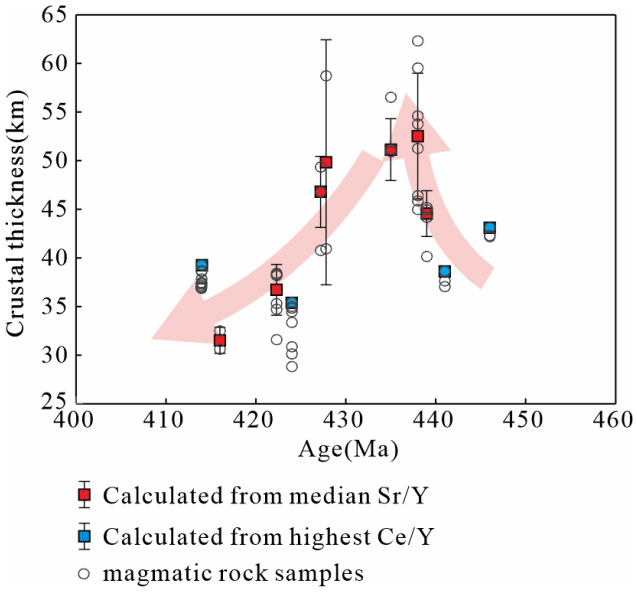


**Figure 13.** Plot of crustal thickness versus age of magmatic rocks for each data subset in the Longshoushan, southwestern Alxa Block. Data are in Table S1.

### 6.3.3 Tectonic evolution of the Longshoushan in the early Paleozoic

A notable feature of the Longshoushan is the large volume of late Ordovician–Silurian magmatic rocks (Fig. 2). Based on the statistics and analysis of U–Pb ages and geochemical data of these rocks, three stages of magmatic activities can be defined (Fig. 14).

In the first stage (460–444 Ma), the magmatic rocks are all acidic rocks (except one mafic rock,; Fig. 14) and calc-alkaline (alkali-calcic) granites (Fig. 4), which is consistent with the magmatic rock assemblage formed in a subduction environment (Song et al., 2015; Wang et al., 2020). Additionally, the 461–444 Ma magmatic rocks are enriched in LREEs and LILEs, depleted in HREEs and HFSEs, and exhibit significant negative anomalies of Nb, Ta, P, and Ti (Fig. 5a and b), which are consistent with the characteristics of arc-derived magmas (Jahn et al., 1999; Li et al., 2016). Hence, the magmatic events during this period are related to slab subduction. During this period, there are some A-type granites, which are possibly related to the extension caused by the rollback of the subducting slab. This phenomenon has been observed in the Central Asian Orogenic Belt and in eastern Australia (Cawood et al., 2011; Wu et al., 2021).

In the North Qilian Orogenic Belt, there are two ophiolite belts, the Northern Ophiolite Belt (NOB) and the Southern Ophiolite Belt (SOB), separated by the North Qilian Volcanic Arc (NQVA). Allen et al. (2023) identified the oceans

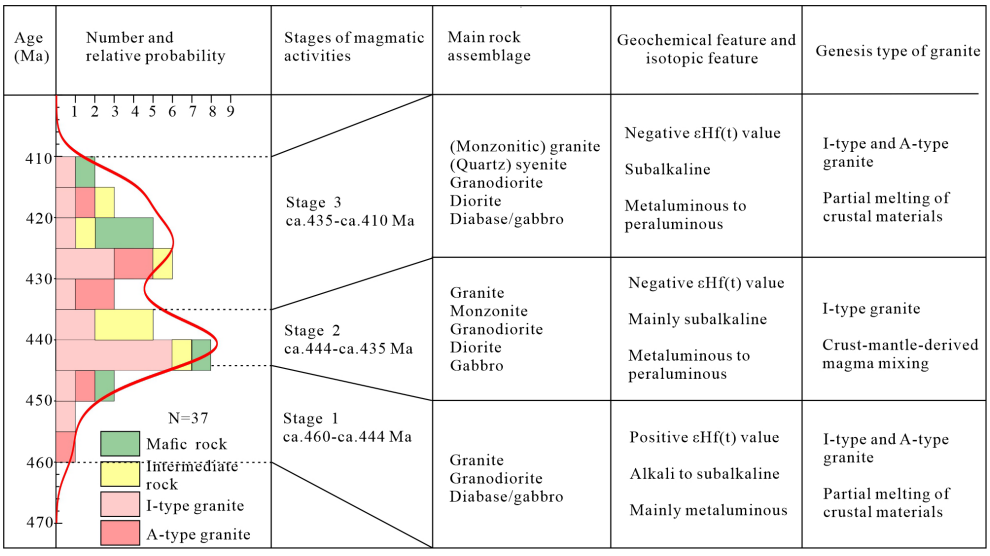


**Figure 14.** Integrated column of magmatism evolution of the early Paleozoic in the Longshoushan area. On the left is a histogram of age distribution of early Paleozoic magmatic rocks in the Longshoushan area. Data are in Table S1.

represented by these two ophiolite belts as the main Proto-Tethys ocean and the North Qilian back-arc basin (NQ bab), respectively. The Dachadaban tholeiite–boninite suite (517–487 Ma) and Laohushan IAB-type boninite (492–488 Ma) are considered to have been formed by the northward subduction of the Proto-Tethys on the southern side of the North Qilian Volcanic Arc (NQVA) (Xia et al., 2012; Fu et al., 2022). Their formation ages indicate that this subduction was already underway in the mid-late Cambrian (Fig. 15a). Under this tectonic setting, intense magmatic activity occurred in the North Qilian Volcanic Arc (NQVA) and the Southern Ophiolite Belt (SOB) during the mid- to late Cambrian and early Ordovician. In comparison, the initiation age of the northward subduction of the North Qilian back-arc basin (NQ bab) is later. The formation age of SSZ-type ophiolites (gabbro, basalt, and plagiogranite) formed in the northward subduction of the North Qilian back-arc basin (NQ bab) is 454–448 Ma (Fu et al., 2020), while the age of metamorphism of the Laohushan boninite related to this subduction event is ~ 455 Ma (Fu et al., 2022). Therefore, there is no intense Cambrian magmatic activity in the Northern Ophiolite Belt (NOB), Hexi Corridor (HC), and Longshoushan. The magmatic activity in these areas gradually intensified in the middle–late Ordovician, which is consistent with the North Qilian back-arc basin (NQ bab) undergoing northward subduction by this time (Fig. 15b).

In the second stage (444–435 Ma), compared to the first stage of magmatic activity, the intensity of the 444–435 Ma magmatic activity significantly increased, and the rocks have higher total alkali content (Fig. 4a and b). In this stage, although calc-alkaline granitic magmatism was still dominant, there are also some alkaline rocks. In addition, as previously mentioned, the ~ 440 Ma monzogranite and ~ 439 Ma K-feldspar granite were formed by crust- and mantle-derived magma mixing. During this period, mantle-derived intermediate–basic rocks also existed in the Longshoushan (Fig. 7). Therefore, there was mantle-derived magmatic activity in the Longshoushan from 444 to 435 Ma. The above magmatic rock assemblage is consistent with the post-collisional magmatic rock assemblage formed after a major ocean closed (Zhang et al., 2019; Wang et al., 2020). Noting that the meaning of post-collisional has multiple interpretations, the post-collisional stage refers to the stage after the initial collision between continental plates or between continental plates and island arcs in this study (Liegeois et al., 1998). In this study, the zircon $\varepsilon$Hf(t) values of the monzogranite and K-feldspar granite are primarily negative, with a minimum value reaching −16.27. As shown in Fig. 10, the Hf isotope characteristics indicate a significant decrease in zircon $\varepsilon$Hf(t) during the 444–435 Ma period compared to the previous stage (Fig. 10), reflecting the increasing contribution of ancient continental crust components in the magma source region. This phenomenon is also consistent with the variations in magmatic rocks during the transition from subduction to collision (Li et al., 2023). As shown in Fig. 13, significant crustal thickening occurred in the Longshoushan during the period of 444–437 Ma. This is consistent with the fact that the monzogranite and K-feldspar granite in this study were formed through partial melting near the base of the thickened lower crust, with source pressures approximately between 0.8 and 1.5 GPa. In addition, research has shown that thickened crust also occurred in the Hexi Corridor (HC),the Northern Ophiolite Belt (NOB), and the North Qilian Volcanic Arc (NQVA) on the southern side of the Longshoushan during 450–430 Ma (Zhang et al., 2017; Yang et al., 2019). The above phenomena are consistent with the short-

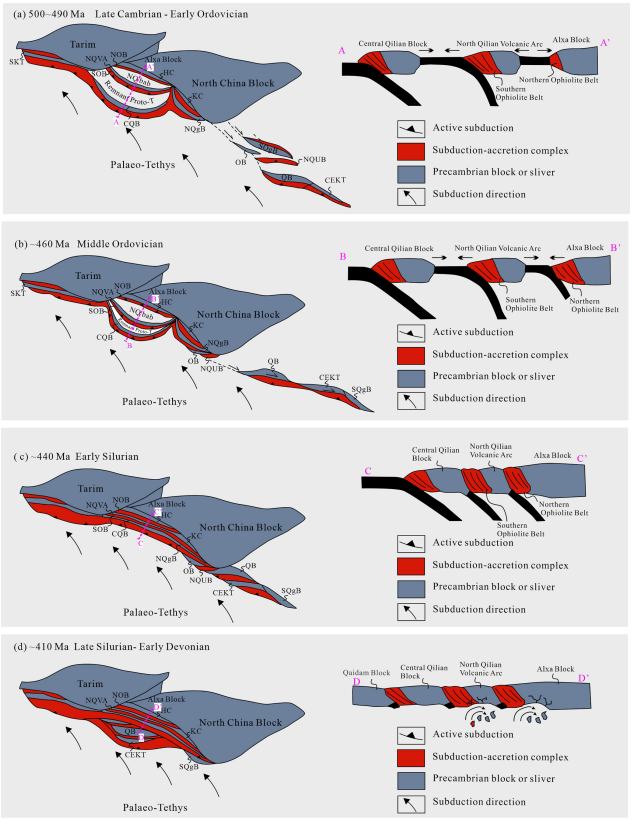


**Figure 15.** Tectonic model illustrating the four stages of evolution of the Central China Orogenic Belt. Abbreviations are as follows. CEKT: Central East Kunlun Terrane. CQB: Central Qilian Block. HC: Hexi Corridor. KC: Kuangping Complex. NOB: Northern Ophiolite Belt. NQgB: North Qinling Belt. NQUB: North Qaidam Ultra High-pressure Belt. NQVA: North Qilian Volcanic Arc. OB: Oulongbuluke Block. SKT: South Kunlun Terrane. SOB: Southern Ophiolite Belt. SQgB: South Qinling Block. QB: Qaidam Block.

ening and thickening of continental crust caused by the closure of ocean basins and subsequent continent–continent collision (Li et al., 2023). In addition, the latest arc-type magmatic rocks in the North Qilian Orogenic Belt were found to have formed at 446 Ma (Wang et al., 2005). Silurian molasse rocks are widely distributed and unconformably overlie pre-Silurian strata in this orogenic belt (Song et al., 2013; Xia et al., 2016; Zeng et al., 2021). Hence, it is generally believed that the closure of the NQ bab occurred at the end of the Ordovician (∼ 444 Ma; Song et al., 2013; Zeng et al., 2021). Therefore, the Longshoushan transitioned from a subduction environment to a post-collisional environment from ∼ 444 Ma (Fig. 15c).

Collectively, the characteristics of the Longshoushan rocks from 444–435 Ma are similar to the signatures of the magmatism after 440 Ma in the North Qaidam Ultrahigh-Pressure Belt (NQUB) (Allen et al., 2023), presently ∼ 500 km to the southwest of the Longshoushan. This coincidence in timing and evolution requires either a chance juxtaposition of separate arcs and continents across separate subduction zones or, and more likely in our view, the duplication of sections of what was once a single subduction and collision system.

In the third stage (435–410 Ma), during the evolution of orogenic events, calc-alkaline granites are commonly replaced gradually by high-silica alkaline to peralkaline magmatic rocks (Fig. 4), representing the transition from the post-collisional compressional environment to an extensional environment (Liégeois et al., 1998; Bonin, 2004). In the Longshoushan, the 444–435 Ma magmatic rocks are mainly high-potassium calc-alkaline I-type granite (Fig. 14). However, the proportion of alkaline rock series significantly increased and multiple A-type granites appeared during 435–410 Ma, indicating the characteristics of an intracontinental extensional environment. During this period, a significant number of mantle-derived mafic dykes were intruded, which also reflects an extensional setting (Zeng et al., 2021). Therefore, the Longshoushan transitioned from a post-collisional compressional environment to an extensional setting at ∼ 435 Ma. As discussed earlier, the transition in crustal thickness from thickening to thinning in the Longshoushan also occurred at ∼ 435 Ma, which is consistent with the inferred stress changes in the study area (although we cannot rule out efficient erosion as the cause of crustal thinning). The driver for the proposed extension is not clear, but it would have been enhanced by a crust with initially greater thickness than normal.

There are two different views regarding the mechanism of the transition from a compressional environment to an extensional environment in the North Qilian Orogenic Belt: slab break-off (Xia et al., 2016; Zeng et al., 2021) and lithospheric delamination (Yu et al., 2015; Zhang et al., 2017). Studies have shown that the mantle-derived magmas in this stage mainly derived from the enriched lithospheric mantle, indicating that the lithospheric mantle in the Longshoushan has not been completely delaminated (Zeng et al., 2021). Small-scale delamination of hydrated lithosphere is a possible generation mechanism (Kaisalaniemi et al., 2014) (Fig. 15d). A complementary mechanism is adiabatic melting during extension and lithospheric thinning, supported by the observations of crustal thinning over time. These mechanisms are not mutually exclusive. While we cannot fully rule out slab break-off, we note modelling studies that suggest it does not normally generate significant magmatism (Freeburn et al., 2017).

## 7 Conclusions

- LA-ICP-MS zircon U–Pb dating indicates that the monzogranite and the K-feldspar granite in the east of Longshoushan formed at $440.8 \pm 2.1$ Ma (MSWD = 1.6) and $439.4 \pm 2.0$ Ma (MSWD = 0.88), respectively.
- The monzogranite and K-feldspar granite in the east of the Longshoushan were generated through various degrees of mixing between crustal-derived magma from the thickened lower crust- and mantle-derived magma and then underwent extensive fractional crystallization with removal of plagioclase, K-feldspar, amphibole, biotite, rutile, monazite, and allanite.
- Based on the temporal and spatial distribution of the magmatic rocks in the Longshoushan, we propose a three-stage tectonic evolution model. (1) 461 to 445 Ma: the northward subduction of NQ bab resulted in the development of arc-type magmatic rocks. (2) 444 to 435 Ma: the closure of the NQ bab and subsequent continent–continent collision resulted in significant crustal thickening in the study area. (3) 435 to 410 Ma: tectonics transitioned from a collisional compressional environment to an extensional environment, evidenced by crustal thinning at this time.

*Data availability.* The data are presented in the Supplement.

*Supplement.* The supplement related to this article is available online at https://doi.org/10.5194/se-16-179-2025-supplement.

*Author contributions.* RZ: conceptualization, methodology, and writing (original draft). HS: writing (original draft) and visualization. MBA: writing (review and editing. HS: visualization. CZ: visualization. JY: funding acquisition.

*Competing interests.* The contact author has declared that none of the authors has any competing interests.

*Disclaimer.* Publisher's note: Copernicus Publications remains neutral with regard to jurisdictional claims made in the text, published maps, institutional affiliations, or any other geographical representation in this paper. While Copernicus Publications makes every effort to include appropriate place names, the final responsibility lies with the authors.

*Acknowledgements.* We thank M. Santosh, Zhijie Song, and Liangpeng Deng for constructive reviews and useful suggestions. We are also grateful to Qixing Ai and Yuhua Wang for their help with the fieldwork.

*Financial support.* This research has been supported by the Jiangxi Provincial Natural Science Foundation (grant no. 20232BAB213061); the China Uranium Industry Co. LTD. – East China University of Technology Innovation Partnership Foundation (grant no. 2023NRE- 45 LH-12); the National Nature Science Foundation of China (grant nos. 42030809, 42262017, 42002095, and 42162013); the China Scholarship Council (grant no. 202008360018); and the Open Research Fund Program of Key Laboratory of Metallogenic Prediction of Nonferrous Metals and Geological Environment Monitoring (Central South University), Ministry of Education (grant no. 2022YSJS10).

*Review statement.* This paper was edited by Andrea Di Muro and reviewed by Jan Wijbrans and Huan Li.

## References

Allen, M. B., Song, S. G., Wang, C., Zeng, R. Y., and Wen, T.: An oblique subduction model for closure of the Proto-Tethys and Palaeo-Tethys oceans and creation of the Central China Orogenic Belt, Earth-Sci. Rev., 104385, https://doi.org/10.1016/j.earscirev.2023.104385, 2023.

Bonin, B.: Do coeval mafic and felsic magmas in post-collisional to within-plate regimes necessarily imply two contrasting, mantle and crustal, sources?, Lithos, 78, 1–24, https://doi.org/10.1016/j.lithos.2004.04.042, 2004.

Burnham, A. D. and Berry, A. J.: Formation of Hadean granites by melting of igneous crust, Nat. Geosci., 10, 457–461, https://doi.org/10.1038/ngeo2942, 2017.

Cawood, A. P., Pisarevsky, A. S., and Leitch, C. E.: Unraveling the New England orocline, east Gondwana accretionary margin, Tectonics, 30, 1–15, https://doi.org/10.1029/2011TC002864, 2011.

Chappell, B. W. and White, A. J. R.: I- and S-type granites in the Lachlan Fold Belt, Geol. Soc. Am. Spec. Pap., 272, 1–26, https://doi.org/10.1130/SPE272-p1, 1992.

Dan, W., Li, X. H., Guo, J. H., Liu, Y., and Wang, X. C.: Paleoproterozoic evolution of the eastern Alxa Block, westernmost North China: Evidence from in situ zircon U-Pb dating and Hf-O isotopes, Gondwana Res., 21, 838–864, https://doi.org/10.1016/j.gr.2011.09.004, 2012.

Dan, W., Li, X. H., Wang, Q., Wang, X. C., and Liu, Y.: Neoproterozoic S-type granites in the Alxa Block, westernmost North China and tectonic implications: in situ zircon U-Pb-Hf-O isotopic and geochemical constraints, Am. J. Sci., 14, 110–153, https://doi.org/10.2475/01.2014.04, 2014.

Dan, W., Li, X. H., Wang, Q., Wang, X. C., Wyman, D. A., and Liu, Y.: Phanerozoic amalgamation of the Alxa Block and North China Craton: Evidence from Paleozoic granitoids, U-Pb geochronology and Sr-Nd-Pb-Hf-O isotope geochemistry, Gondwana Res., 32, 105–121, https://doi.org/10.1016/j.gr.2015.02.011, 2016.

Dong, C. Y., Liu, D. Y., Li, J. J., Wan, Y. S., Zhou, H. Y., Li, C. D., Yang, Y. H., and Xie, L. W.: New evidence for the timing of the formation of the western segment of the Khondalite Belt in the North China Craton: SHRIMP dating Hf isotopic composition of zircons from the Bayanwula Helan Shan region, Chinese

Sci. Bull., 16, 1913–1922, https://doi.org/10.3321/j.issn:0023-074x.2007.16.012, 2007.

Duan, F. H., Zhi, Q., Li, Y. J., Xiao, H., Wang, P. L., and Gao, J. P.: Petrogenesis and geodynamic setting of the Late Carboniferous granodioriteporphyry in Miaoergou pluton, southern West Junggar, Acta Petrol. Sin., 37, 1159–1176, https://doi.org/10.18654/1000-0569/2021.04.12, 2021.

Ferry, J. M. and Watson, E. B.: New thermodynamic models and revised calibrations for the Ti-in-zircon and Zr-in-rutile thermometers, Contrib. Mineral. Petrol., 154, 429–437, https://doi.org/10.1007/s00410-007-0201-0, 2007.

Foley, S. F., Barth, M. G., and Jenner, G. A.: Rutile/Melt partition coefficients for trace elements and an assessment of the influence of rutile on the trace element characteristics of subduction zone magmas, Geochim. Cosmochim. Ac., 64, 933–938, https://doi.org/10.1016/S0016-7037(99)00355-5, 2000.

Freeburn, R., Bouilhol, P., Maunder, B., Magni, V., and Hunen, J. V.: Numerical models of the magmatic processes induced by slab break off, Earth Planet. Sci. Lett., 478, 203–213, https://doi.org/10.1016/j.epsl.2017.09.008, 2017.

Frost, C. D. and Frost, B. R.: On ferroan (A-type) granitoids: Their compositional variability and modes of origin, J. Petrol., 52, 39–53, https://doi.org/10.1093/petrology/egq070, 2011.

Fu, D., Kusky, T. M., Wilde, S. A., Windley, B. F., Polat, A., Huang, B., and Zhou, Z. P.: Structural anatomy of the early Paleozoic Laohushan ophiolite and subduction complex: Implications for accretionary tectonics of the Proto-Tethyan North Qilian orogenic belt, northeastern Tibet, Geol. Soc. Am. Bull., 132, 2175–2201, https://doi.org/10.1130/B35442.1, 2020.

Fu, D., Kusky, T. M., Wilde, S. A., Windley, B. F., Polat, A., Huang, B., and Zhou, Z. P.: Boninitic blueschists record subduction initiation and subsequent accretion of an arc-forearc in the northeast Proto-Tethys Ocean, Geology, 50, 10–15, https://doi.org/10.1130/G49457.1, 2022.

Gong, J. H., Zhang, J. X., Wang, Z. Q., Yu, S. Y., Li, H. K., and Li, Y. S.: Origin of the Alxa Block, western China: New evidence from zircon U-Pb geochronology and Hf isotopes of the Longshoushan Complex, Gondwana Res., 36, 359–375, https://doi.org/10.1016/j.gr.2015.06.014, 2016.

Griffin, W. L., Wang, X., Jackson, S. E., Pearson, N. J., O'Reilly, S. Y., Xu, X. X., and Zhou, X. M.: Zircon chemistry and magma mixing, SE China: In-situ analysis of Hf isotopes, Tonglu and Pingtan igneous complexes, Lithos, 61, 237–269, https://doi.org/10.1016/S0024-4937(02)00082-8, 2002.

Harris, N. B. W., Inger, S., and Xu, R. H.: Cretaceous plutonism in Central Tibet: an example of post-collision magmatism?, J. Volcanol. Geotherm. Res., 44, 21–32, https://doi.org/10.1016/0377-0273(90)90009-5, 1990.

He, H. Y., Li, Y. L., Wang, C. S., Han, Z. P., Ma, P. F., and Xiao, S. Q.: Petrogenesis and tectonic implications of Late Cretaceous highly fractionated I-type granites from the Qiangtang block, central Tibet, J. Asian Earth Sci., 176, 337–352, https://doi.org/10.1016/j.jseaes.2019.02.022, 2019.

Hoskin, P. W. O. and Schaltegger, U.: The composition of zircon and igneous and metamorphic petrogenesis, Rev. Mineral. Geochem., 53, 27–62, https://doi.org/10.2113/0530027, 2003.

Hu, F. Y., Ducea, M. N., Liu, S. W., and Chapman, J. B.: Quantifying Crustal Thickness in Continental Collisional Belts: Global Perspective and a Geologic Application, Sci. Rep., 7, 1–10, https://doi.org/10.1038/s41598-017-07849-7, 2017.

Hu, Z. C., Liu, Y. S., Gao, S., Liu, W. G., Zhang, W., and Tong, X. R.: Improved in situ Hf isotope ratio analysis of zircon using newly designed X skimmer cone and jet sample cone in combination with the addition of nitrogen by laser ablation multiple collector ICP-MS, J. Anal. At. Spectrom., 27, 1391–1399, https://doi.org/10.1039/C2JA30078H, 2012.

Hui, J., Zhang, K. J., Zhang, J., Qu, J. F., Zhang, B. H., Zhao, H., and Niu, P. F.: Middle-late Permian high-K adakitic granitoids in the NE Alxa block, northern China: Orogenic record following the closure of a Paleo-Asian oceanic branch?, Lithos, 400–401, 106379, https://doi.org/10.1016/j.lithos.2021.106379, 2021.

Jahn, B. M., Wu, F. Y., Lo, C. H., and Tsai, C. H.: Crust-mantle interaction induced by deep subduction of the continental crust: geochemical and Sr-Nd isotopic evidence from post-collisional mafic-ultramafic intrusions of the Northern Dabie complex, central China, Chem. Geol., 157, 119–146, https://doi.org/10.1016/S0009-2541(98)00197-1, 1999.

Karsli, O., Dokuz, A., Uysal, İ., Aydin, F., Chen, B., Kandemir, R., and Kandemir, R.: Relative contributions of crust and mantle to generation of Campanian high-K calc-alkaline I-type granitoids in a subduction setting, with special reference to the Harşit Pluton, Eastern Turkey, Contrib. Mineral. Petrol., 160, 467–487, https://doi.org/10.1007/s00410-010-0489-z, 2010.

Kong, H., Li, H., Wu, Q. H., Xi, X. S., Dick, J. M., and Gabo-Ratio, J. A. S.: Co-development of Jurassic I-type and A-type granites in southern Hunan, South China: Dual control by plate subduction and intraplate mantle upwelling, Chem. Erde-Geochem., 78, 500–520, https://doi.org/10.1016/j.chemer.2018.08.002, 2018.

Li, B., Jiang, S. Y., Lu, A. H., Zhao, H. X., Yang, T. L., and Hou, M. L.: Zircon U-Pb dating, geochemical and Sr-Nd-Hf isotopic characteristics of the Jintonghu monzonitic rocks in western Fujian Province, South China: Implication for Cretaceous crust-mantle interactions and lithospheric extension, Lithos, 260, 413–428, https://doi.org/10.1016/j.lithos.2016.05.002, 2016.

Li, C. D., Zhang, Q., Miao, L. C., and Meng, X. F.: Mesozoic high-Sr, low-Y and low-Sr, low-Y types granitoids in the northern Hebeiprovince: Geochemistry and petrogenesis and its relation to mineralization of gold deposits, Acta Petrol. Sin., 20, 269–284, https://doi.org/10.1016/j.sedgeo.2004.01.002, 2004.

Li, H., Sun, H. S., Wu, J. H., Evans, N. J., Xi, X. S., Peng, N. L., Cao, J. Y., and Gabo-Ratio, J. A. S.: Re-Os and U-Pb geochronology of the Shazigou Mo polymetallic ore field, Inner Mongolia: Implications for Permian-Triassic mineralization at the northern margin of the North China Craton, Ore Geol. Rev., 83, 287–299, https://doi.org/10.1016/j.oregeorev.2016.12.010, 2017.

Li, J. Y., Zhang, J., and Qu, J. F.: Amalgamation of North China Craton with Alxa Block in the Late of Early Paleozoic: Evidengce from Sedmentary Sequences in the Niushou Mountain, Ningxia Hui Autonomous Region, NW China, Geol. Rev., 58, 208–214, https://doi.org/10.16509/j.georeview.2012.02.014, 2012.

Li, S., Wang, T., Xiao, W. J., and Ho, Q. L.: Tectono-magmatic evolution from accretion to collision in the southern margin of the Central Asian Orogenic Belt, Acta Petrol. Sin., 39, 1261–1275, https://doi.org/10.18654/1000-0569/2023.05.03, 2023.

Liégeois, J. P., Navez, J., Hertogen, J., and Black, R.: Contrasting origin of post-collisional high-K calc-alkaline and shoshonitic versus alkaline and peralkaline granitoids, The use of sliding

normalization, Lithos, 45, 1–28, https://doi.org/10.1016/S0024-4937(98)00023-1, 1998.

Liu, Q., Zhao, G. C., Han, Y. G., Eizenhöfer, P. R., Zhu, Y. L., Hou, W. Z., and Zhang, X. R.: Timing of the final closure of the Paleo-Asian Ocean in the Alxa Terrane: Constraints from geochronology and geochemistry of Late Carboniferous to Permian gabbros and diorites, Lithos, 274–275, 19–30, https://doi.org/10.1016/j.lithos.2016.12.029, 2017.

Liu, Q., Zhao, G. C., Sun, M., Han, Y. G., Eizenhofer, P. R., Hou, W. Z., Zhang, X. R., Zhu, Y. L., Wang, B., and Liu, D. X.: Early Paleozoic subduction processes of the Paleo-Asian Ocean: Insights from geochronology and geochemistry of Paleozoic plutons in the Alxa Terrane, Lithos, 262, 546–560, https://doi.org/10.1016/j.lithos.2016.07.041, 2016.

Liu, Q. Q., Li, H., Shao, Y. J., Girei, M. B., Jiang, W. C., Yuan, H. M., and Zhang, X.: Age, genesis, and tectonic setting of the Qiushuwan Cu-Mo deposit in East Qinling (Central China): constraints from Sr-Nd-Hf isotopes, zircon U-Pb and molybdenite Re-Os dating, Ore Geol. Rev., 132, 103998, https://doi.org/10.1016/j.oregeorev.2021.103998, 2021.

Liu, W. H., Spier, C., Niu, Y. B., Liu, X. D., Yan, J., Wang, K. X., and Pan, J. Y.: Magma mixing in the genesis of the Qingshanbao granitoids in the Longshoushan area: Implications for the tectonic evolution of the North Qilian orogenic belt, NW China, Geol. J., 56, 4594–4617, https://doi.org/10.1002/gj.4195, 2021.

Li, Y. L., Zhou, H. W., Brouwer, F. M., Xiao, W. J., Wijbrans, J. R., and Zhong, Z. Q.: Early Paleozoic to Middle Triassic bivergent accretion in the Central Asian Orogenic Belt: insights from zircon U-Pb dating of ductile shear zones in central Inner Mongolia, China, Lithos, 205, 84–111, https://doi.org/10.1016/j.lithos.2014.06.017, 2014.

Ma, L., Jiang, S. Y., Dai, B. Z., Jiang, Y. H., Hou, M. L., Pu, W., and Xu, B.: Multiple sources for the origin of Late Jurassic Linglong adakitic granite in the Shandong Peninsula, eastern China: Zircon U-Pb geochronological, geochemical and Sr-Nd-Hf isotopic evidence, Lithos, 162–163, 251–263, https://doi.org/10.1016/j.lithos.2013.01.009, 2013.

Maniar, P. D. and Piccoli, P. M.: Tectonic discrimination of granitoids, Geol. Soc. Am. Bull., 101, 635–643, https://doi.org/10.1130/0016-7606(1989)101<0635:TDOG>2.3.CO;2, 1989.

Mantle, G. W. and Collins, W. J.: Quantifying crustal thickness variations in evolving orogens: Correlation between arc basalt composition and Moho depth, Geology, 36, 87–90, https://doi.org/10.1130/G24095A.1, 2008.

Middlemost, E. A. K.: Naming materials in the magma/igneous rock system, Earth-Sci. Rev., 37, 215–224, https://doi.org/10.1016/0012-8252(94)90029-9, 1994.

Pearce, J. A., Harris, N. B. W., and Tindle, A. G.: Trace Element Discrimination Diagrams for the Tectonic Interpretation of Granitic Rocks, J. Petrol., 25, 956–983, https://doi.org/10.1093/petrology/25.4.956, 1984.

Qi, J. W., Zhang, S. M., Yang, C. S., Lan, D. C., and Wang, L. L.: The LA-lCP-MS zircon U-Pb age of the pegmatoidal alaskite and its relationshipwith uranium mineralization in Hongshiquan area, Gansu Province, Geol. Bull., 38, 562–572, https://doi.org/CNKI:SUN:ZQYD.0.2019-04-009, 2019.

Schiano, P., Monzier, M., Eissen, J. P., Martin, H., and Koga, K. T.: Simple mixing as the major control of the evolution of volcanic suites in the Ecuadorian Andes, Contrib. Mineral. Petrol., 160, 297–312, https://doi.org/10.1007/s00410-009-0478-2, 2010.

Schiller, D. and Finger, F.: Application of Ti-in-zircon thermometry to granite studies: problems and possible solutions, Contrib. Mineral. Petrol., 174, 51, https://doi.org/10.1007/s00410-019-1585-3, 2019.

Shi, X. J., Wang, T., Zhang, L., Castro, A., Xiao, X. C., Tong, Y., Zhang, J. X., Guo, L., and Yang, Q. D.: Timing, petrogenesis and tectonic setting of the Late Paleozoic gabbro-granodiorite-granite intrusions in the Shalazhashan of northern Alxa: Constraints on the southernmost boundary of the Central Asian Orogenic Belt, Lithos, 208–209, 158–177, https://doi.org/10.1016/j.lithos.2014.08.024, 2014.

Skjerlie, K. P. and Johnston, A. D.: Vapor-absent melting at 10 kbar of a biotite-and amphibole-bearing tonalitic gneiss: implications for the generation of A-type granites, Geology, 20, 263–266, https://doi.org/10.1130/0091-7613(1992)020<0263:VAMAKO>2.3.CO;2, 1992.

Song, S. G., Niu, Y. L., Su, L., and Xia, X. H.: Tectonics of the North Qilian Orogen, NW China, Gondwana Res., 23, 1378–1401, https://doi.org/10.1016/j.gr.2012.02.004, 2013.

Song, S. G., Wang, M. J., Wang, C., and Niu, Y. L.: Magmatism during continental collision, subduction, exhumation and mountaincollapse in collisional orogenic belts and continental net growth: A perspective, Sci. China Earth Sci., 58, 1284–1304, https://doi.org/10.1007/s11430-015-5102-x, 2015.

Sun, H. S., Li, H., Danišík, M., Xia, Q. L., Jiang, C. L., Wu, P., Yang, H., Fan, Q. R., and Zhu, D. S.: U-Pb and Re-Os geochronology and geochemistry of the Donggebi Mo deposit, Eastern Tianshan, NW China: Insights into mineralization and tectonic setting, Ore Geol. Rev., 86, 584–599, https://doi.org/10.1016/j.oregeorev.2017.03.020, 2017.

Sun, S. S. and Mcdonough, W. F.: Chemical and isotopic systematics of oceanic basalts: implications for mantle composition and processes, Geol. Soc. Lond. Spec. Publ., 42, 313–345, https://doi.org/10.1144/GSL.SP.1989.042.01.19, 1989.

Sylvester, P. J.: Post-collisional strongly peraluminous granites, Lithos, 45, 29–44, https://doi.org/10.1016/S0024-4937(98)00024-3, 1998.

Tang, Y. L., Shi, Y., Hu, X. M., Liu, X. J., and Huang, C. W.: Petrogenesis of Early Paleozoic I-type granitoids in the Wuyi-Yunkai Orogen, South China: Implications for the tectono-magmatic evolution of the Cathaysia Block, J. Asian Earth Sci., 220, 104906, https://doi.org/10.1016/j.jseaes.2021.104906, 2021.

Trail, D., Watson, E. B., and Tailby, N. D.: Ce and Eu anomalies in zircon as proxies for the oxidation state of magmas, Geochim. Cosmochim. Ac., 97, 70–87, https://doi.org/10.1016/j.gca.2012.08.032, 2012.

Wang, C. Y., Zhang, Q., Qian, Q., and Zhou, M. F.: Geochemistry of the Early Paleozoic Baiyin Volcanic Rocks (NW China): Implications for the Tectonic Evolution of the North Qilian Orogenic Belt, J. Geol., 113, 83–94, https://doi.org/10.1086/425970, 2005.

Wang, T., Tong, Y., Zhang, L., Li, S., Huang, H., Zhang, J. J., Guo, L., Yang, Q. D., Hong, D. W., Donskaya, T., Gladkochub, D., and Tserendash, N.: Phanerozoic granitoids in the middle and eastern parts of CentralAsia and their tectonic significance, J. Asian Earth Sci., 145, 368–392, https://doi.org/10.1016/j.jseaes.2017.06.029, 2017.

Wang, Z. Z., Chen, X. H., Li, B., Zhang, Y. P., and Xu, S. L.: The discovery of the Paleoproterozoic syenite in Helishan, Gansu Province, and its implications for the tectonic attribution of the Alxa Block, Geol. China, 46, 1094–1104, https://doi.org/10.12029/gc20190510, 2019.

Wang, Z. Z., Chen, X. H., Shao, Z. G., Li, B., Ding, W. C., Zhang, Y. P., Wang, Y. C., Zhang, Y. Y., Xu, S. L., and Qin, X.: Petrogenesis of the Late Silurian-Early Devonian granites in the Longshoushan-Helishan area, Gansu Province, and its tectonic implications for the Early Paleozoicevolution of the southwestern Alxa Block, Acta Geol. Sin., 94, 2243–2261, https://doi.org/10.19762/j.cnki.dizhixuebao.2020027, 2020.

Wang, Z. Z., Han, B., Feng, L. X., and Liu, B.: Geochronology, geochemistry and origins of the Paleozoic-Triassic plutons in the Langshan area, western Inner Mongolia, China, J. Asian Earth Sci., 97, 337–351, https://doi.org/10.1016/j.jseaes.2014.08.005, 2015.

Watson, E. B. and Harrison, T. M.: Zircon saturation revisited: temperature and composition effects in variety of crustal magma types, Earth Planet. Sci. Lett., 64, 295–304, https://doi.org/10.1016/0012-821X(83)90211-X, 1983.

Watson, E. B. and Harrison, T. M.: Zircon Thermometer Reveals Minimum Melting Conditions on Earliest Earth, Science, 308, 841–844, https://doi.org/10.1126/science.1120977, 2005.

Wei, Q. Q., Hao, L. B., Lu, J. L., Zhong, Y. Y., Zhao, X. Y., and Shi, H. L.: LA-MC-ICP-MS Zircon U-Pb Dating of Hexipu Granite and lts Geologica Implications, Bull. Mineral., Petrol. Geochem., 32, 729–735, 2013.

Whalen, J. B., Currie, K. L., and Chappell, B. W.: A-type granites: geochemical characteristics, discrimination and petrogenesis, Contrib. Mineral. Petrol., 95, 407–419, https://doi.org/10.1007/BF00402202, 1987.

Wolf, M. B. and London, D.: Apatite dissolution into peraluminous haplogranitic melts:An experimental study of solubilities and mechanism, Geochim. Cosmochim. Ac., 58, 4127–4145, https://doi.org/10.1016/0016-7037(94)90269-0, 1994.

Wu, D. D., Li, S., Chew, D., Liu, T. X., and Guo, D. H.: Permian-Triassic magmatic evolution of granitoids from the southeastern Central Asian Orogenic Belt: lmplications for accretion leading to collision, Sci. China Earth Sci., 64, 788–806, https://doi.org/10.1007/S11430-020-9714-5, 2021.

Wu, F. Y., Liu, X. C., Ji, W. Q., Wang, J. M., and Yang, L.: Highly fractionated granites: recognition and research, Sci. China Earth Sci., 60, 1201–1219, https://doi.org/10.1007/s11430-016-5139-1, 2017.

Xia, L. Q., Li, X. M., Yu, J. Y., and Wang, G. Q.: Mid-late neoproterozoic to early paleozoic volcanism and tectonic evolution of the Qilianshan, NW China, Georesj, 9–12, 1–41, https://doi.org/10.1016/j.grj.2016.06.001, 2016.

Xia, X., Song, S., and Niu, Y.: Tholeiite-Boninite terrane in the North Qilian suture zone: Implications for subduction initiation and back-arc basin development, Chem. Geol., 328, 259–277, https://doi.org/10.1016/j.chemgeo.2011.12.001, 2012.

Xiao, B., Chen, H. Y., Hollings, P., Han, J. S., Wang, Y. F., Yang, J. T., and Cai, K. D.: Magmatic evolution of the Tuwu-Yandong porphyry Cu belt, NW China: Constraints from geochronology, geochemistry and Sr-Nd-Hf isotopes, Gondwana Res., 43, 74–91, https://doi.org/10.1016/j.gr.2015.09.003, 2017.

Xiao, W. J., Windley, B. F., Sun, S., Li, J. L., Huang, B. C., Han, C. M., Yuan, C., Sun, M., and Chen, H. L.: A tale of amalgamation of three Permo-Triassic collage systems in Central Asia: oroclines, sutures, and terminal accretion, Annu. Rev. Earth Planet. Sci., 43, 477–507, https://doi.org/10.1146/annurev-earth-060614-105254, 2015.

Xue, S., Ling, M. X., Liu, Y. L., Zhang, H., and Sun, W. D.: The genesis of early Carboniferous adakitic rocks at the southern margin of the Alxa Block, North China, Lithos, 278–281, 181–194, https://doi.org/10.1016/j.lithos.2017.01.012, 2017.

Yang, H., Zhang, H. F., Xiao, W. J., Luo, B. J., Gao, Z., Tao, L., Zhang, L. Q., and Guo, L.: Petrogenesis of Early Paleozoic high Sr/Y intrusive rocks from the North Qilian orogen: Implication for diachronous continental collision, Lithosphere, 12, 53–73, https://doi.org/10.1130/L1129.1, 2019.

Yu, S. Y., Zhang, J. X., Qin, H. P., Sun, D. Y., Zhao, X. L., Cong, F., and Li, Y. S.: Petrogenesis of the early Paleozoic low-Mg and high-Mg adakitic rocks in the North Qilian orogenic belt, NW China: Implications for transition from crustal thickening to extension thinning, J. Asian Earth Sci., 107, 122–139, https://doi.org/10.1016/j.jseaes.2015.04.018, 2015.

Yuan, W. and Yang, Z. Y.: The Alashan Terrane did not amalgamate with North China block by the Late Permian: Evidence from Carboniferous and Permian paleomagnetic results, J. Asian Earth Sci., 104, 145–159, https://doi.org/10.1016/j.jseaes.2014.02.010, 2015.

Zeng, R. Y., Lai, J. Q., Mao, X. C., Li, B., Ju, P. J., and Tao, S. L.: Geochemistry, zircon U-Pb dating and Hf isotopies composition of Paleozoic granitoids in Jinchuan, NW China: Constraints on their petrogenesis, source characteristics and tectonic implication, J. Asian Earth Sci., 121, 20–33, https://doi.org/10.1016/j.jseaes.2016.02.009, 2016.

Zeng, R. Y., Lai, J. Q., Mao, X. C., Li, B., Zhang, J. D., Bayless, R., and Yang, L. Z.: Paleoproterozoic multiple tectonothermal events in the Longshoushan area, Western North China Craton and their geological implication: evidence from geochemistry, zircon U-Pb geochronology and Hf isotopes, Minerals, 8, 361, https://doi.org/10.3390/MIN8090361, 2018.

Zeng, R. Y., Lai, J. Q., Mao, X. C., Xiao, W. Z., Yan, J., Zhang, C. G., and Xiao, W. Z.: Geochemistry and zircon ages of the Yushigou diabase in the Longshoushan area, Alxa Block: implications for crust-mantle interaction and tectonic evolution, Geol. Mag., 158, 685–700, https://doi.org/10.1017/S0016756820000783, 2021.

Zeng, R. Y., Allen, M. B., Mao, X. C., Lai, J. Q., Yan, J., and Wan, J. J.: Whole-rock and zircon evidence for evolution of the Late Jurassic high Sr/Y Zhoujiapuzi granite, Liaodong Peninsula, North China Craton, Solid Earth, 13, 1259–1280, https://doi.org/10.5194/se-2021-129, 2022.

Zhang, B., Guo, F., Zhang, X. B., Wu, Y. M., Wang, G. Q., and Zhao, L.: Early Cretaceous subduction of Paleo-Pacific Ocean in the coastal region of SE China: Petrological and geochemical constraints from the mafic intrusions, Lithos, 334–335, 8–24, https://doi.org/10.1016/j.lithos.2019.03.010, 2019.

Zhang, D. H., Wei, J. H., Fu, L. B., Chen, H. Y., Tan, J., Li, Y. J., Shi, W. J., and Tian, N.: Formation of the Jurassic Changboshan-Xieniqishan highly fractionated I-type granites, northeastern China: implication for the partial melting of juvenile crust in-

duced by asthenospheric mantle upwelling, Geol. J., 50, 122–138, https://doi.org/10.1002/gj.2531, 2015.

Zhang, J. J., Wang, T., Zhang, L., Tong, Y., Zhang, Z. C., Shi, X. J., Guo, L., Huang, H., Yang, Q. D., Huang, W., Zhao, J. X., Ye, K., and Hou, J. Y.: Tracking deep crust by zircon xenocrysts within igneous rocks from the northern Alxa, China: Constraints on the southern boundary of the Central Asian Orogenic Belt, J. Asian Earth Sci., 108, 150–169, https://doi.org/10.1016/j.jseaes.2015.04.019, 2015.

Zhang, J. J., Wang, T., Castro, A., Zhang, L., Shi, X. J., Tong, Y., Zhang, Z. C., Guo, L., Yang, Q. D., and Iaccheri, L. M.: Multiple Mixing and Hybridization from Magma Source to Final Emplacement in the Permian Yamatu Pluton, the Northern Alxa Block, China, J. Petrol., 157, 183–197, https://doi.org/10.1007/BF01765318, 2016.

Zhang, J. X. and Gong, J. H.: Revisiting the nature and affinity of the Alxa Block, Acta Petrol. Sin., 34, 940–962, doi:10.2018-04-008, 2018.

Zhang, J. X., Gong, J. H., Yu, S. Y., Li, H. K., and Hou, K. J.: Neoarchean-Paleoproterozoic multiple tectonothermal events in the western Alxa block, North China Craton and their geological implication: Evidence from zircon U-Pb ages and Hf isotopic composition, Precambrian Res., 235, 36–57, https://doi.org/10.1016/j.precamres.2013.05.002, 2013.

Zhang, L., Zhang, H., Hawkesworth, C., Luo, B., and Yang, H.: Mafic rocks from the southern Alxa block of Northwest China and its geodynamic evolution in the Paleozoic, J. Geol. Soc., 178, 2020–038, https://doi.org/10.1144/jgs2020-038, 2021.

Zhang, L., Wang, T., Zhang, J. J., Shi, X. J., Ren, H. D., Yang, Q. D., Tong, Y., and Guo, L.: Revisiting the boundary between the Central Asian Orogenic Belt and North China Craton in Alxa area, China: Insights from zircon U-Pb ages and Hf isotopes of Phanerozoic granitoids, Gondwana Res, 119, 119–137, https://doi.org/10.1016/j.gr.2023.03.011, 2023.

Zhang, L. Q., Zhang, H. F., Zhang, S. S., Xiong, Z. L., Luo, B. J., Yang, H., Pan, F. B., Zhou, X. C., Xu, W. C., and Guo, L.: Lithospheric delamination in post-collisional setting: Evidence from intrusive magmatism from the North Qilian orogen to southern margin of the Alxa block, NW China, Lithos, 288–289, 20–34, https://doi.org/10.1016/j.lithos.2017.07.009, 2017.

Zhang, Q., Wang, Y., Li, C. D., Wang, Y. L., Jin, W. J., and Jia, X. Q.: Granite classification on the basis of Sr and Yb contents and its implications, Acta Petrol. Sin., 22, 2249–2269, https://doi.org/10.3969/j.issn.1000-0569.2006.09.001, 2006.

Zhang, Q., Jin, W. J., Li, C. D., and Wang, Y. L.: Revisiting the new classification of granitic rocks based on whole-rock Sr and Yb contents:ndex, Acta Petrol. Sin., 26, 985–1015, https://doi.org/CNKI:SUN:YSXB.0.2010-04-002, 2010.

Zhang, W. and Hu, Z. C.: Estimation of Isotopic Reference Values for Pure Materials and Geological Reference Materials, At. Spectrosc., 41, 93–102, https://doi.org/10.46770/AS.2020.03.001, 2020.

Zhou, X. C., Zhang, H. F., Luo, B. J., Pan, F. B., Zhang, S. S., and Guo, L.: Origin of high Sr/Y-type granitic magma-tism in the southwestern of the Alxa Block, Northwest China, Lithos, 256–257, 211–227, https://doi.org/10.1016/j.lithos.2016.04.021, 2016.

Zong, K. Q., Klemd, R., Yuan, Y., He, Z. Y., Guo, J. L., Shi, X. L., Liu, Y. S., Hu, Z. C., and Zhang, Z. M.: The assembly of Rodinia: The correlation of early Neoproterozoic (ca. 900 Ma) high-grade metamorphism and continental arc formation in the southern Beishan Orogen, southern Central Asian Orogenic Belt (CAOB), Precambrian Res., 290, 32–48, https://doi.org/10.1016/j.precamres.2016.12.010, 2017.

Zorpi, M. J., Coulon, C., Orsini, J. B., and Cocirta, C.: Magma mingling, zoning and emplacement in calc-alkaline granitoid plutons, Tectonophysics, 157, 315–329, https://doi.org/10.1016/0040-1951(89)90147-9, 1989.